UNIVERSITY OF OKLAHOMA

GRADUATE COLLEGE

INJECTION EXPERIMENTS ON ROCKS UNDER TRIAXIAL CONDITION WITH ACOUSTIC EMISSION MONITORING

A THESIS

SUBMITTED TO THE GRADUATE FACULTY

in partial fulfillment of the requirements for the

Degree of

MASTER OF SCIENCE

By

MOSTAFA ESKANDARI HALVAEI
Norman, Oklahoma
2016

INJECTION EXPERIMENTS ON ROCKS UNDER TRIAXIAL CONDITION WITH ACOUSTIC EMISSION MONITORING

A THESIS APPROVED FOR THE
MEWBOURNE SCHOOL OF PETROLEUM AND GEOLOGICAL ENGINEERING

BY

_____
Dr. Ahmad Ghassemi, Chair

_____
Dr. Ahmad Jamili

_____
Dr. Mashhad Fahes

DEDICATION

To my wife, my son, and myself

Acknowledgements

I would like to thank my committee chair, Dr. Ghassemi, and my committee members, Dr. Jamili and Dr. Fahes, for their guidance and support. Special thanks to Dr. Ghassemi who supported me in my graduate study. And thanks to my colleague and friend Rohit Bakshi who provided help and expertise through my experiments. It was my pleasure working with him.

Also Thanks to my friends, our group members, colleagues and faculty and staff of department of Petroleum Engineering making my time at University of Oklahoma a great experience.

Table of Contents

List of Tables

List of Figures

Abstract

This work presents the results of a series of triaxial- injection experiments carried out on two basalt cores from the Newberry geothermal field well GEO-N2 and a Mississippi lime stone. A combination of triaxial and injection experiments were performed on the cores to characterize their goemechanical properties and to better understand their response to stimulation treatment. The first GEO-N2 sample (sample A) was axially loaded to a vertical stress of 10000 psi at a strain rate of $1x10^{-5}$ strains/sec while maintaining an effective confining pressure of 3500 psi and a temperature of 90 ^{o}C. Nitrogen gas was injected at a pressure of 2000 psi. Sample didn't fail. Then the pore pressure increased to 4500 psi resulting in an effective confining pressure of 1000 psi. However the sample still did not fail due to injection. Since the intention of the test was to create the Mohr - Coulomb envelope by performing a multistage triaxial test, the deviatoric stress did not get increased to fracture the sample and sample fractured by multistage triaxial test.

The triaxial-injection test performed on the second GEO-N2 sample (sample B) same as the first GEO-N2 sample with the same procedure and configurations. For the last part of the test, the intention was to fail the rock with injection. Therefore, at the moment of the turning point on the volumetric strain curve, the axial load was held constant and the sample was fractured by injecting nitrogen gas in to it. The sample temperature was 90^{o} C.

The Mississippi lime stone sample (sample C) was axially loaded to a vertical stress of 6000 psi at a strain rate of $1x10^{-5}$ strains/sec while maintaining an effective confining pressure of 2000 psi. Nitrogen gas was injected at a pressure of 2000 psi. Sample didn't

fail. Then the pore pressure increased to 3300 psi resulting in an effective confining pressure of 700 psi. However the sample still did not fail due to injection. For the last part of the test, the intention was to fail the rock with injection. Therefore, at the moment of the turning point on the volumetric strain curve, the axial load was held constant and the sample was tried to be fractured by injecting nitrogen gas in to it. However it did not fractured and sample C got fractured by compression.

Fluid flow was maintained across the samples throughout the experiments while stress, strain and acoustic emissions were recorded. Rock deformation and acoustic emissions data were monitored and analyzed, and the locations of events were recorded and they correlate with the fracture location in the samples. The result showed that all three samples have high value of Young's modulus over a 40 GPA. Sample A and B experiments were conducted at elevated temperatures to investigate the rock response to thermal stresses. Heat didn't influence the elastic properties very much in these rocks. It is estimated that higher temperatures (>300 C) would probably create this effect. And about 0.03% strain was observed in hydrostatic heating of the sample. Sample C is from an oil field which is not hot and the tests on this sample were not performed at high temperature.

Chapter 1: Introduction

Problem Statement

Creation of conductive fluid flow pathways and heat exchange are the bases of EGS development. This study is mainly an experimental research and the main objectives were as follows;

1. To prepare experimental setup and conduct a triaxial-injection test to help understand the rock response to stimulation
2. Collect all possible geomechanical information from the sample. This includes Mohr-Coulomb envelope, sample compressive strength, elastic parameters etc.

The cores for this study are from the well GEO- N2, drilled at Newberry geothermal field and a Mississippi lime sample from Oklahoma. Experiments on GEO- N2 samples have been performed under heated conditions.

The GEO- N2 well is located about 2.8 km from the western rim of the Newberry volcano caldera in Oregon, U.S.A. The cores from the GEO N2 had a diameter of 0.0635 m (2.5 inches) and were cored to obtain two samples whose length to diameter ratios varied from 1.5:1 to 2:1 (Details are provided in the relevant section). The Mississippi lime sample had a diameter of 0.1008 m (4 inches) and the length to diameter ratio of 1.41 and is from a depth of a 5893 ft.

Mineral composition and pore scale characterization were performed using XRD and thin sections of the core. A variety of laboratory tests have been conducted on the plugs to determine rock strength (triaxial and injection tests), velocity data (shear and compressional), elastic properties, acoustic emissions and stress-dependent porosity and permeability.

Literature Review

Triaxial Test

Triaxial test is used to measure the deformation properties and strength of cylindrical rock specimen as a function of the confining pressure. The stresses applied to the specimen while running the triaxial compression test are presented in Figure 1. The confining stress σ_c is applied by building the pressure up using the fluid surrounding the specimen which is also equal to the radial stress σ_r, or minor principal stress σ_3. The deviator stress q is generated by applying an axial strain ε_a to the specimen. The axial stress σ_a, or major principal stress σ_1 is the addition of the deviator stress to the confining stress in the axial direction. The minor principal stress state is said to be isotropic when $\sigma_1 = \sigma_3$, and anisotropic when $\sigma_1 \neq \sigma_3$.

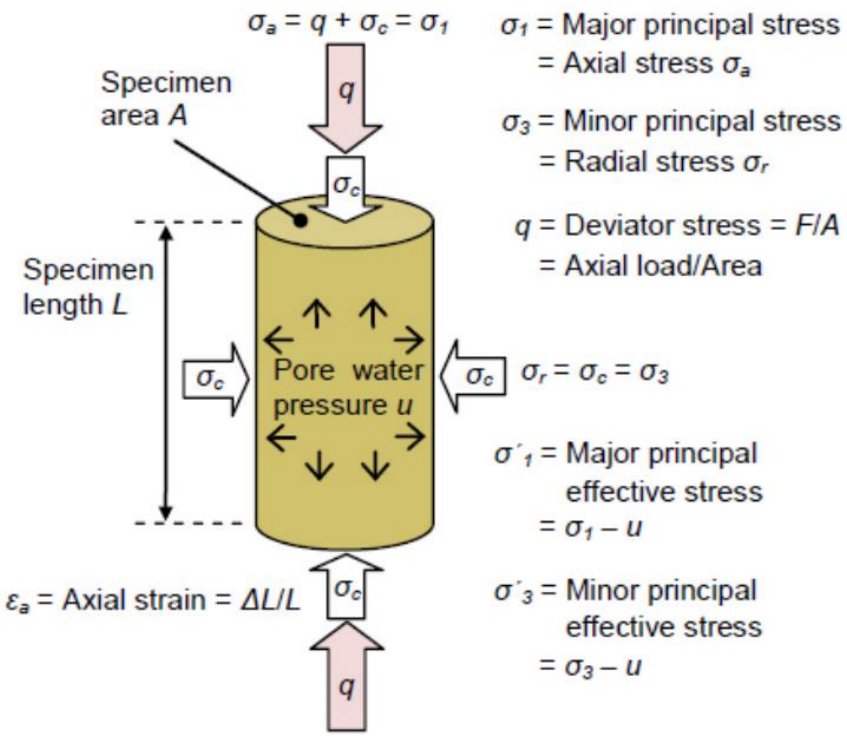

Figure 1. Stress State on Triaxial Compression Test

Different technical equipment and machinery needed for triaxial test can be listed as below;

- Triaxial cell – Parts of the triaxial cell are pressure vessel, loading piston, seals, platens with spherical seating, hydraulic connections, and bleeder hole. Platens needs to be place at bottom and top of the specimen. These platens should have a Rockwell hardness of more than C30 (ISRM standards). The diameter of the platens should be between 1 to 1.02 times the diameters of the specimen. The thickness of the top and bottom platens should be at least one third of the sample diameter and surfaces of the platens should be polished and flat in the range of 0.01 mm.
- Axial load applying and controlling device – A rigid loading machine for applying and measuring the axial load should be used with as high capacity to fail the specimen at desired confining pressure and applying the strains at desired rates.
- Confining pressure applying and controlling device – A hydraulic pump with a sufficient capacity and capable of regulating the pressure within 2% should be used.
- Measuring and recording of loads, pressure and displacement equipment – Axial load should be recorded continuously using a load transducer. Confining pressure should be measured using a pressure transducer or pressure gauges and it is advised to use at least two indicators. Axial displacement measuring and recording should be done with displacement transducer. Having two

displacement transducer at each side of the specimen is recommended. All the reading and measurement should be recorded by a computer for further analysis.

High Temperature Triaxial Test

There are not many laboratory studies on the high temperature triaxial test considering the difficulties and required equipment. One of the early practices has been done by Handin and Hager (1958). Triaxial compression test on dry anhydrite, dolomite, limestone, sandstone, shale, siltstone, slate, and halite single crystal has been done under pressure-temperature conditions simulating depth down to 30,000 feet is done by Handin and Hager (1958). Their results indicates increase of temperature at constant pressure reduces the yield stress. Heating the specimen up to 300°Cat constant pressure increases the ductility of work-hardening rocks which may raise the ultimate strength of the rock.

Most of the times heating eliminates work-hardening and lowers the ultimate strength, so that even though a rock is more ductile, it becomes weaker because of yield stress reduction (Handin and Hager, 1958).

GEO - N2 Newberry

USGS published a document in 1999 with the title of Hydrothermal Mineralogy of Core from Geothermal Drill Holes at Newberry Volcano, Oregon, which described the holes drilled at Newberry Volcano including the GEO - N2 Newberry. The location of the GEO - N2 is on the west flank of Newberry volcano about 2.8 km outside the western rim of the caldera at the elevation of 1,779 m. The reason for choosing the drill site was on the basis of a geophysical anomaly. The sites for most of the west flank drill holes at

Newberry volcano were selected because of electromagnetic or surface resistivity anomalies (Walkey and Swanberg, 1990).

Permeability in Volcanic Rocks

Unlike the lavas, which rapidly cooled upon emplacement, the ignimbrite flows are characterized by a protracted cooling history due to their extraordinary heat retention capacity (P. Sruoga and N. Rubinstein, 2004). They go through two stages: (1) the pre-emplacement stage, which includes vesiculation and fragmentation; and (2) the post-emplacement stage which embraces the cooling and post-cooling history (P. Sruoga and N. Rubinstein, 2004). Cooling history includes welding, Devitrication, Feldspar alteration, Silicification, Vapor-phase crystallization, Quench fragmentation and glass alteration. The post-cooling history includes hydrothermal alteration, weathering, and tectonic deformation. The original petrophysical characteristics can be modified substantially during cooling and in the post-cooling processes. Sruoga and Rubinstein (2004) results show that the highest porosity and permeability occur in rocks with quench fractured glasses and in non-welded ignimbrites with gas-pipe structures, followed by autobrecciated rhyolites and Welded ignimbrites, massive glasses and fresh rhyolites have the lowest permeability.

Chapter 2: Equipment

The two experimental setups having MTS 816 Rock Mechanics Test System and 315 Load Frame are presented in pictures below on Figure 2 and Figure 3. Each component of the experimental system is explained in more detail in the following section.

Figure 2. Multistage Triaxial Experimental Setup with MTS 816 Rock Mechanics Test System

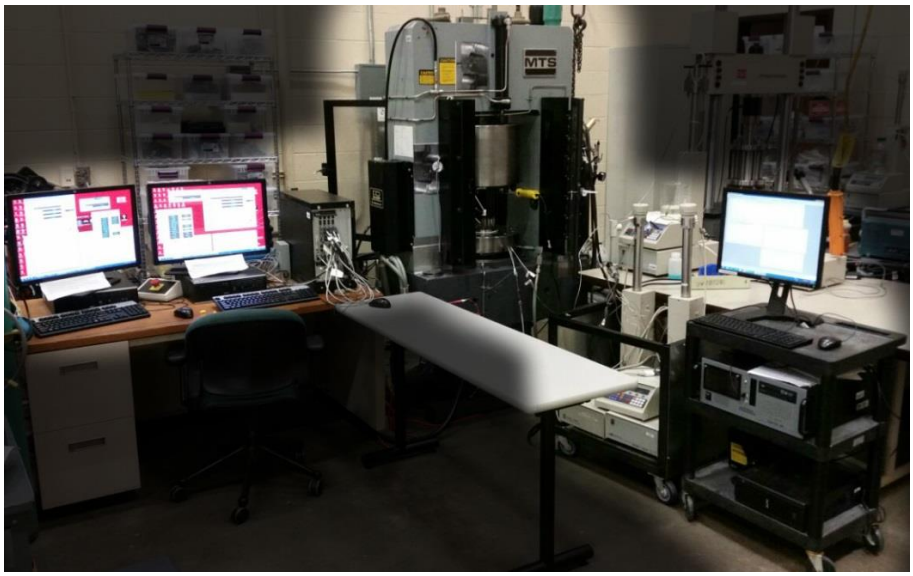

Figure 3. Multistage Triaxial Experimental Setup with 315 Load Frame

The schematic diagram of the system used for the experiments is shown in Figure 4 including triaxial cell, loading unit, fluid circulating system, control station and data acquisition system.

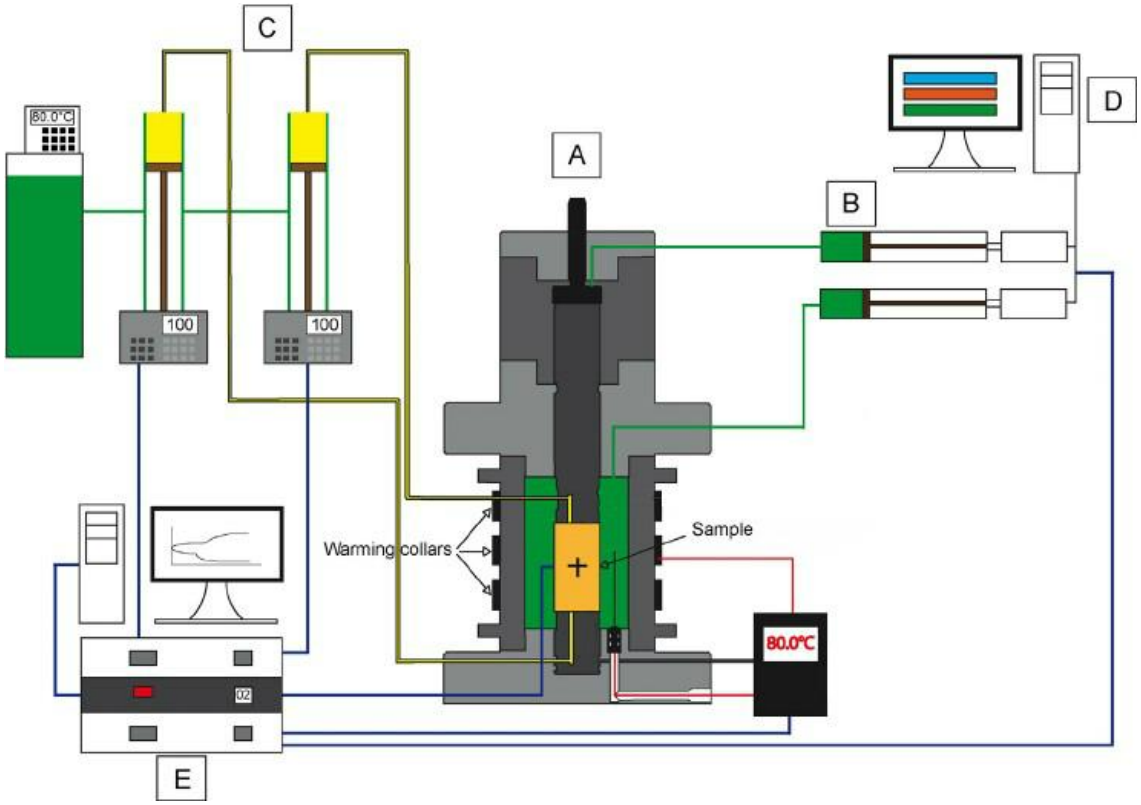

Figure 4. Schematic Diagram of the Experimental System. (A) Triaxial Cell; (B) Loading Unit; (C) Fluid Circulating System; (D) Control Station and (E) Data Acquisition System

MTS Rock Mechanics Test Systems

Both MTS 816 Rock Mechanics Test System and 315 Load Frame were used in the process of different tests. In order to take the dynamic velocity measurements specimens was placed in 315 Load Frame. The permeability measurements, triaxial and injection tests were all performed in the 816 Rock Mechanics Test System. Figure 5 and 6 presents MTS 816 Rock Mechanics Test System and 315 Load Frame.

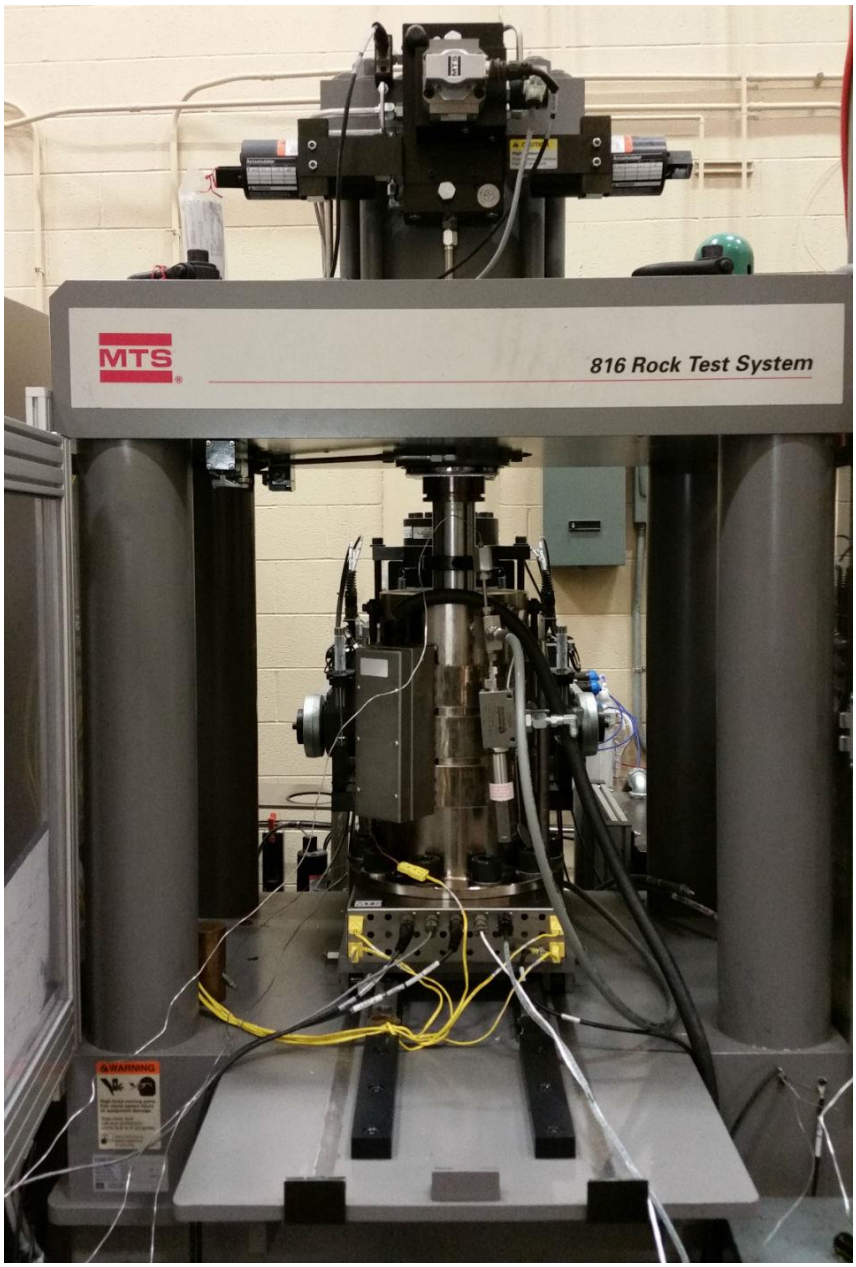

Figure 5. MTS 816 Rock Mechanics Test System

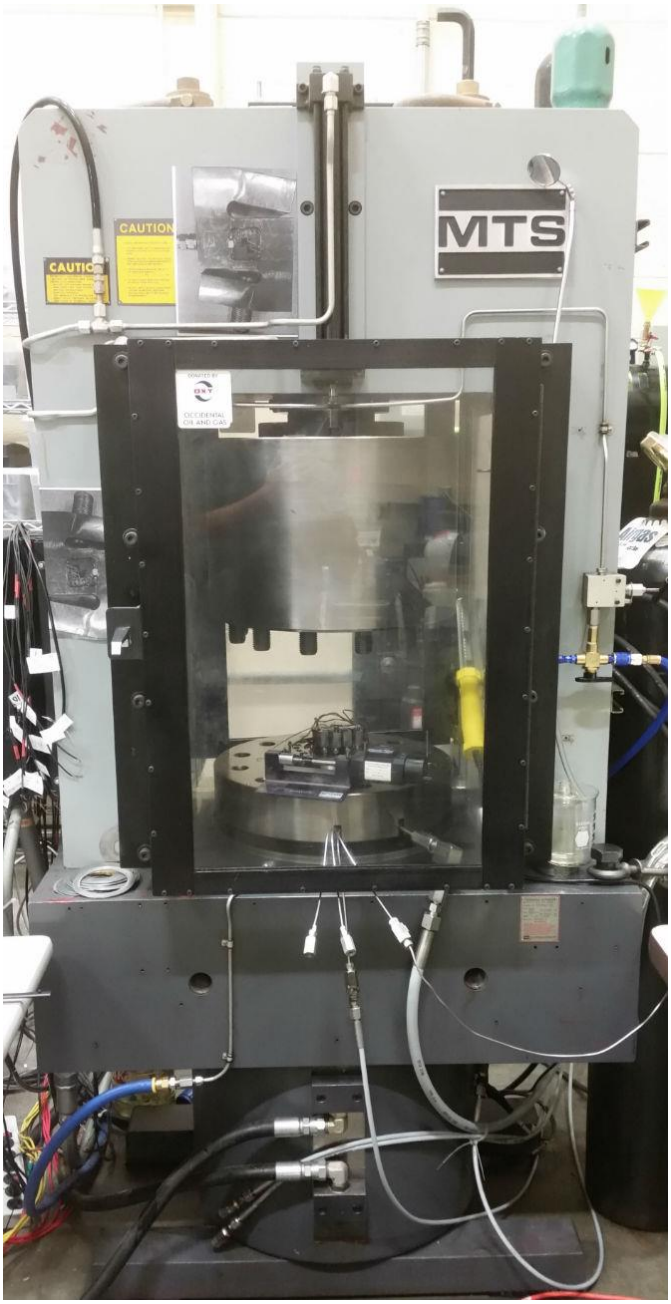

Figure 6. MTS 315 Load Frame

Acoustic Emission (AE) System

The MISTRAS Express-24 channel, Acoustic Emission (AE) system with a frequency range of 1 KHz - 1MHz was used with 8 AE sensors per sample for recording acoustic emissions generated during the triaxial tests. These sensors were Acoustic transducers

with a frequency of 500 kHz. These sensors were attached to the sample using the “E-Z bound instant glue thick” by pushing it to the sample surface with fingers and holding it for 30 seconds.. A preamplifier of 40 dB was applied to all the sensors. The amplitude cut-off on these sensors varied from 55-60 dB; any wave below this amplitude was discarded by the system as noise. Frequency and energy of failure events were also recorded during the tests - these give insights into the nature of the failure; typically, higher confining pressures result in lower energy released during the failure if the rocks become more ductile. A sample rate of 1 MSPS (million samples per second) was used to record the AE information. 3-D location analysis was also performed using AE information - this technique uses the source amplitude and the differences in the time it took the wave to reach the different sensors to arrive at the location of the event. 3-D location is highly dependent upon the rock type, rocks which generate low AE (including certain types of Tuff) typically do not give a good 3-D location response as compared to very brittle rocks which generate high amplitude AE waves during the failure process. AE/MEQ analysis was carried out for all the tests. Figure 7 presents the MISTRAS Industrial Express large PCI Express AE chassis.

Figure 7. MISTRAS Industrial Express large PCI Express AE chassis

Dynamic Velocity Measurements System

Both Compressional and shear velocities were measured using 500 kHz crystals embedded in steel platens placed on top and bottom of the specimen, at hydrostatic pressure of 3.45 MPa (500 psi) to 24.13 MPa (3500 psi). Figure 8 presents the velocity measurement crystals embedded in the platens and Figure 9 presents the Tektronix MDO3022 Mixed Domain Oscilloscope which was used for monitoring the velocity waves. The procedure of dynamic velocity test and determination of rock properties of the results are presented in the appendix.

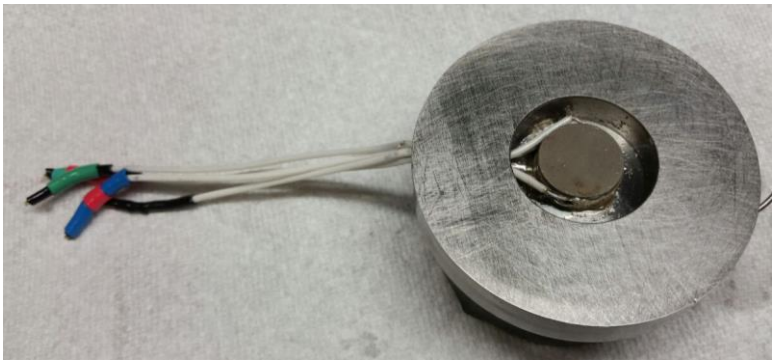

Figure 8. Velocity Measurement Crystals Embedded in Platens

Figure 9. Tektronix MDO3000 Mixed Domain Oscilloscope

Syringe Pump

Different models with different capacities of High precision TELEDYNE ISCO syringe pumps and controllers were used in different stages of the tests. Applying and controlling confining pressure using oil, and applying and controlling pore pressure using nitrogen gas or water was done with these syringe pumps. Figure 10 shows a TELEDYNE ISCO syringe pump and controller.

Figure 10. TELEDYNE ISCO Syringe Pump and Controller

Chapter 3: Preparations

Sample Preparation

Before running any tests on the rocks, the specimens were prepared based on the ISRM standards for parallelism and smoothness. Specimens having all required platens and spacers attached to them to be placed in the MTS 816 Rock Mechanics Test System should be shorter than 11 inches and shorter than 8 inches for 315 Load Frame. Given cores had a diameter of 2.5 inches and based on that the length of 5 inches was cut, which was short enough to fit in the testing systems for running tests. After cutting both surfaces of the specimen was grinded and polished to have an even and smooth surface. Exact diameter, length and weight were measured afterward. Picture of any natural phenomena like healed fractures or mineral formation piece was taken. Also pictures were taken from different angles at each step in front of a scale.

Copper Jacketing

Copper sheet 0.003 mm in thickness purchased from amazon.com was cut in a size covering the specimen sides, 1mm short on each head and was wrapped around the specimen. Rubber band was added to hold the jacket after tightening the jacket. Then the closing side was welded carefully assuring the copper is melted and there is not open gap left. In this process the jacket should not get loose and after welding the jacket should be very tight all around the specimen. Figures 11, 12, and 13 shows the steps of jacketing the specimen with copper sheet.

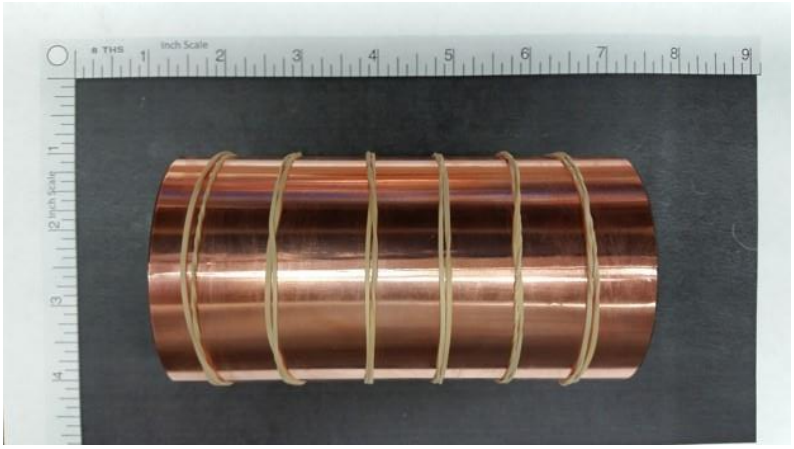

Figure 11. Wrapping the Specimen with Copper Sheet

Figure 12. Welding the Closing Line of Copper Sheet

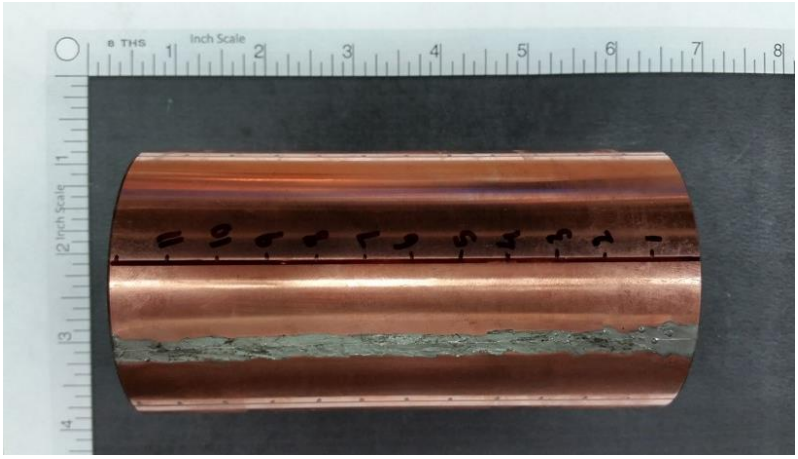

Figure 13. Drawing Vertical Lines and Marking Measurements

Applying Epoxy

To prevent any leakage all the joints should be sealed with epoxy. After placing the platens on two ends of the specimen, using two rounds of self-fusing tape, the specimen and platens stacked on top of each other and stayed standing. 3M Scotch-Weld Epoxy Adhesive tube kit - 2216 B/A Gray with 90 minute work life was used for sample preparation. Epoxy was applied to cover the welding line and self-fusing tape on both heads overlapping the platen and specimen. Figure 14 shows the specimen after epoxy application.

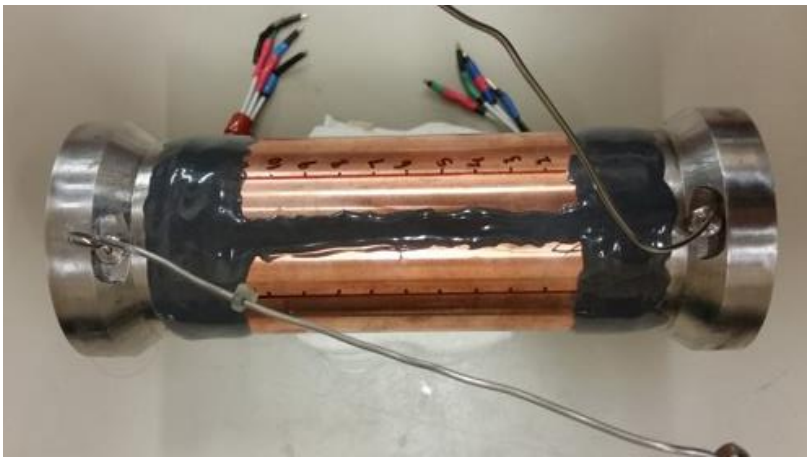

Figure 14. Stress State on Triaxial Compression Test

Attaching Strain Gauges

Proper strain gauge type and size was selected and got prepared by attaching the two wires to be used according to the specimen size. OMEGA strain gauge with the resistance of 120.4 ohms and a gage factor of 2.02 % and Micro-Measurements Division strain gauge with a resistance of 120.0 ohms and a gage factor of 2.09 % were used in the tests. Strain gauge should be attached to the horizontal center line of the specimen. Strain gauges were attached by applying the “E-Z bound instant glue thick” with viscosity of 1500 CPS to the back face of the strain gauges and placing it on the

sample surface and applying pressure. Figure 15 shows the sample strain gauge used in the tests, prepared to be attached, and Figure 16 shows the strain gauge attached to the specimen.

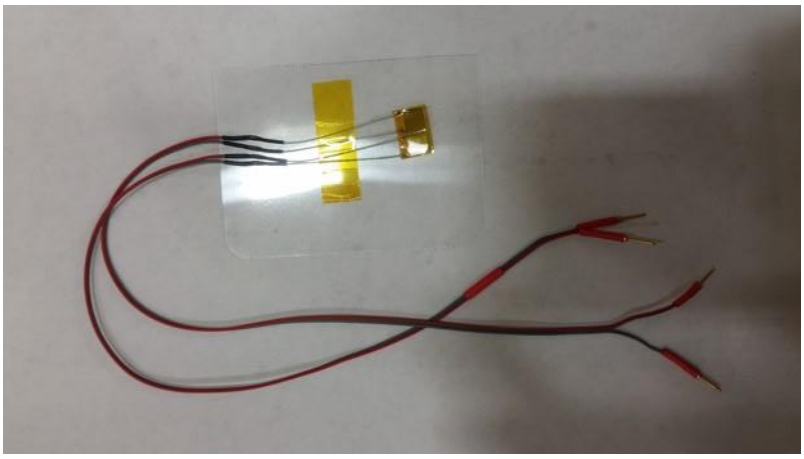

Figure 15. Sample Strain Gauge Prepared to be Attached

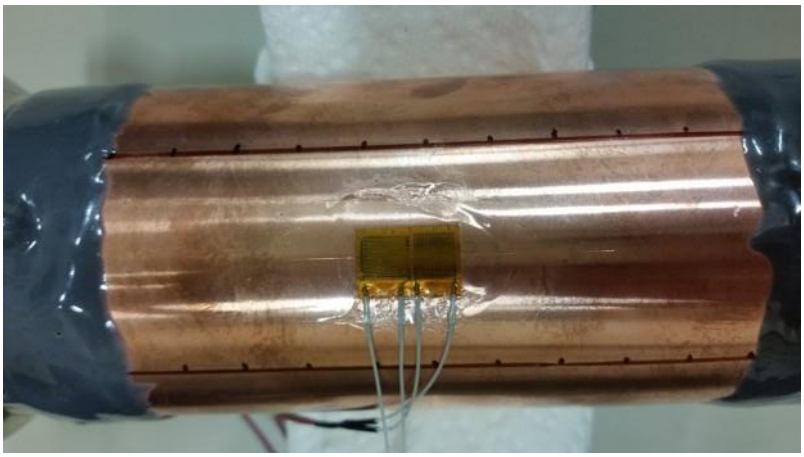

Figure 16. Stain Gauge Attached to the Specimen

Attaching Acoustic Emission (AE) Crystals

It is recommended to spread the Acoustic Emission crystals in a way presented in Figure 17 (Petruzalek, et al. 2012) to capture all the hits by insuring a wider coverage of the sample. However in our tests it was not possible to have the AE crystal on top and bottom of the sample on the platens. Also the radial LVDT chain covered a wide part of

the sample in center and about half inch of sample on each head was covered by epoxy. So the AE crystals were placed closer to the ends of the sample as suggested by Petruzalek, et al. (2012) to cover the missing AE crystal at the ends of the sample.

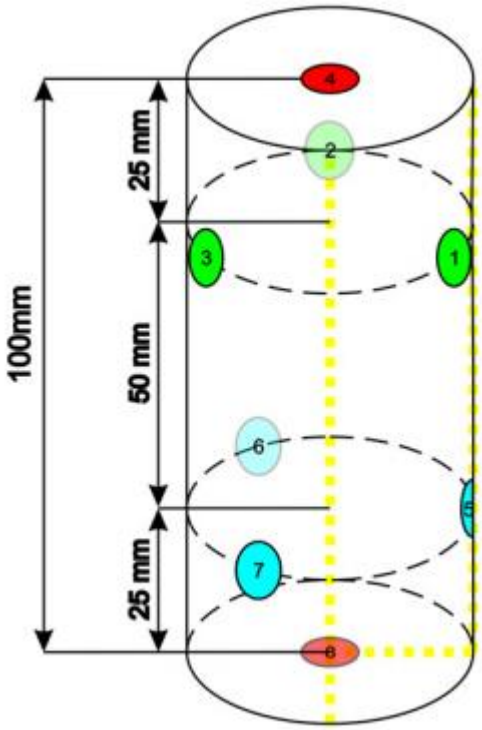

Figure 17. Acoustic Emission crystals location suggested by Petruzalek, et al. (2012)

Acoustic Emission crystals were attached over the copper jacket using the "E-Z bound instant glue thick" by pushing it to the sample surface with fingers and holding it for 30 seconds. Vertical lines were printed on top of the jacket every 60^{o} degree having the welding line in the middle of two of lines, and each line was marked by centimeters from the bottom of the sample to the top (Figure 18). Crystals were attached and each one was labeled and its location was recorded. Figure 19 shows a screenshot of the template I created in excel to record the AE crystal locations and to calculate the 3D

location of them needed to import in to the Mistras software. Crystals used in the test were all 500 kHz sensors.

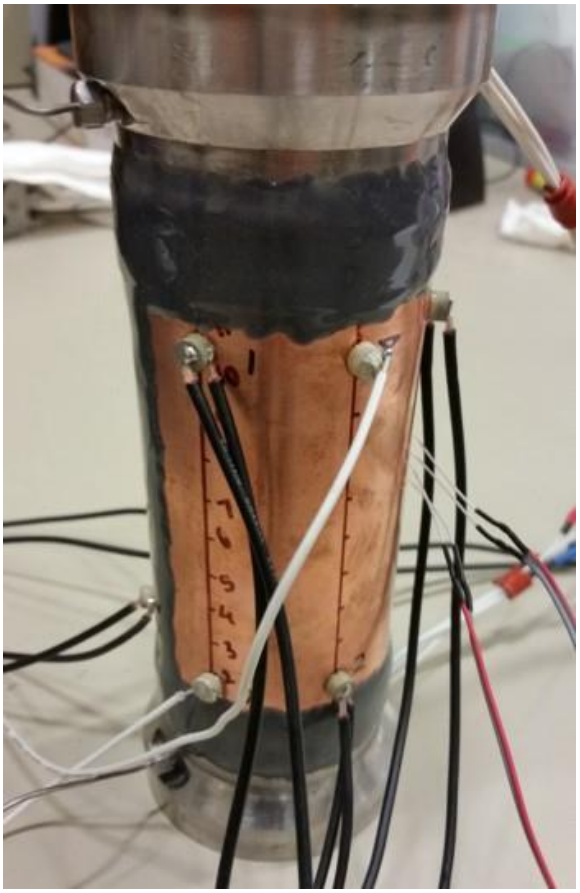

Figure 18. Specimen with Attached Acoustic Emission Crystals

	A	B	C	D	E	F	G	H	I	J	K	L	M	N	O	P	Q
1		A2								Inch				Copy to Mistras Software			
2	Sensor	H mm	H inch	Degree			4,10			x	y	z		Channel	X	Y	Z
3	1	103	4.055118	0		5,11		3,9		0.000	4.055118	1.250		1	0	4.055118	1.249882
4	2	17	0.669291	60		6,12		2,8		1.082	0.669291	0.625		2	1.082429	0.669291	0.624941
5	3	103	4.055118	120			1,7			1.082	4.055118	-0.625		3	1.082429	4.055118	-0.62494
6	4	17	0.669291	180						0.000	0.669291	-1.250		4	1.53E-16	0.669291	-1.24988
7	5	103	4.055118	240						-1.082	4.055118	-0.625		5	-1.08243	4.055118	-0.62494
8	6	17	0.669291	300						-1.082	0.669291	0.625		6	-1.08243	0.669291	0.624941
9	7	17	0.669291	0			mm	in		0.000	0.669291	1.250		7	0	0.669291	1.249882
10	8	103	4.055118	60		L	122.39	4.819		1.082	4.055118	0.625		8	1.082429	4.055118	0.624941
11	9		0	120		D	63.494	2.500		1.082	0	-0.625		9			
12	10		0	180						0.000	0	-1.250		10			
13	11		0	240						-1.082	0	-0.625		11			
14	12		0	300						-1.082	0	0.625		12			

Figure 19. Excel file used to record the AE crystal locations and to calculate the 3D location (Sample B data screenshot)

Chapter 4: Sample A - Tests, Procedures and Results

Sample Description

This sample is a basaltic tuff and light gray in color and has an average depth of 4381.75 ft (uncut core depth of 4378.4 - 4385 ft). It has a length of 127.51 mm (5.02 in) and 63.4 mm (2.5 in) in diameter (L/D ratio of 2:1). The sample is light gray in color and has reddish and white lines running across the sample (Figure 20). It shows no visible fractures - minor or major. It has several white and red veins (healed fractures) on the sample. It also shows few white colored inclusions which vary in size from <1 mm - 5mm in length (Figure 20). The grain structure is fine grained and very well consolidated. Its mineral content is covered in the next section.

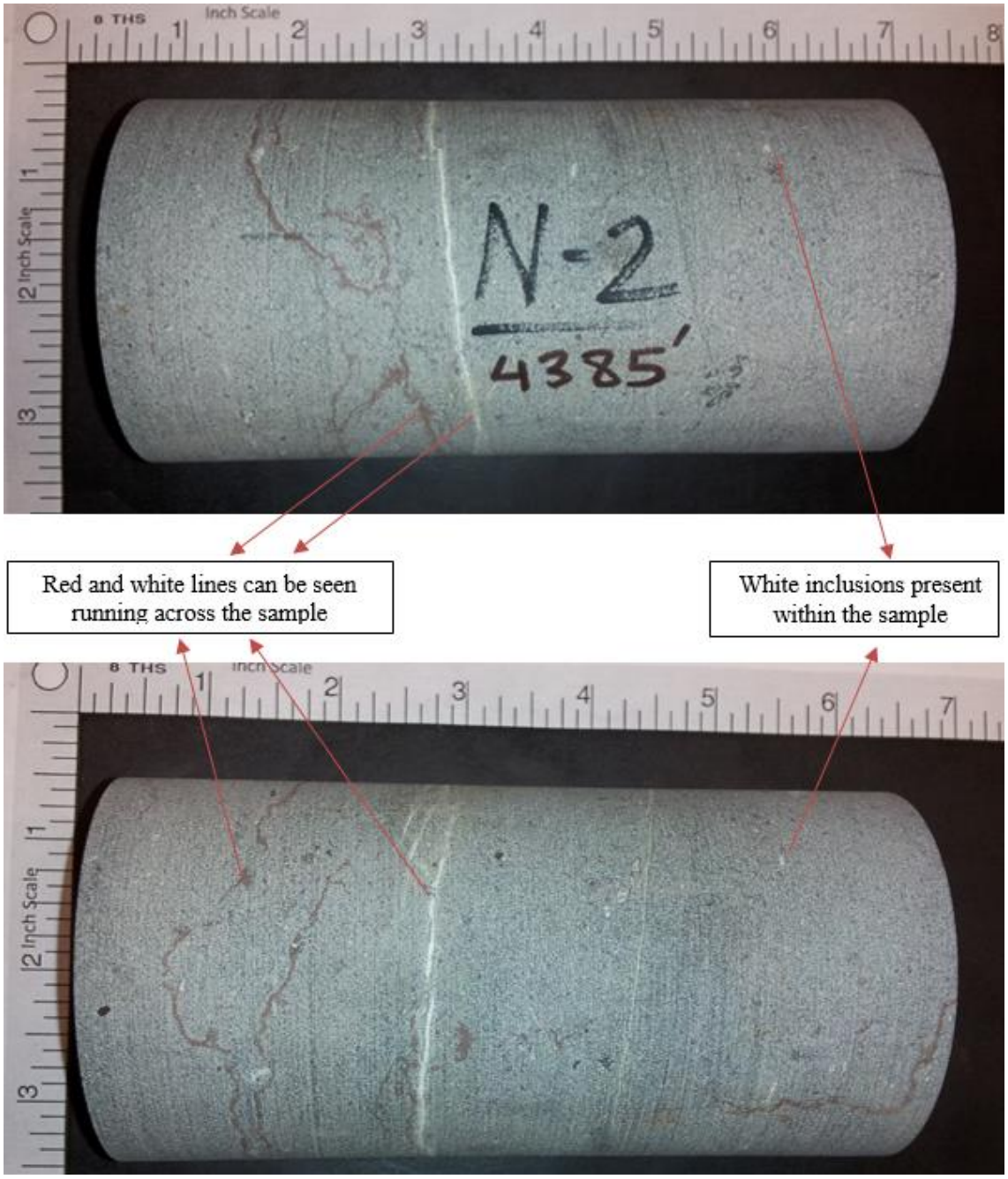

Figure 20. Sample A Cut and Polished Before Test

XRD Results

The XRD test was conducted by Powder X-ray Diffraction Laboratory at University of Oklahoma on the sample and the mineral content and compound composition of the

sample is determined. XRD test is done on about 5 gr of the sample. Table 1 shows the mineral content and table 2 shows the compound composition of sample A.

Table 1. Mineral content in Sample A

Minerals	Weight (%)
Anorthite	28.5
Albite	25.7
Clinochlore	23.2
Corrensite	5.8
Quartz	9.8
Hematite-Ti	2.9
Ferrosillite	3
Fluorite	1

Table 2. Compound Composition in Sample A

Compound	Weight (%)
SiO_2	47.4%
Al_2O_3	25.9%
Fe_2O_3	10.5%
Na_2O	4.7%
MgO	4.1%
CaO	3.7%
TiO_2	0.2%

Dynamic Velocity Measurements

Dynamic velocity tests were carried out with axially placed compressional and shear crystals of frequency 500 Hz. Measurements were carried out at the desired final confining pressure (3500 psi). Appendix A explains how to measure the dynamic velocity. Figure 21 and Figure 22 show a screenshot of the oscilloscope measuring the

P-wave and S-wave travel time for sample A at 3500 psi confining pressure. Results are summarized in Table 3.

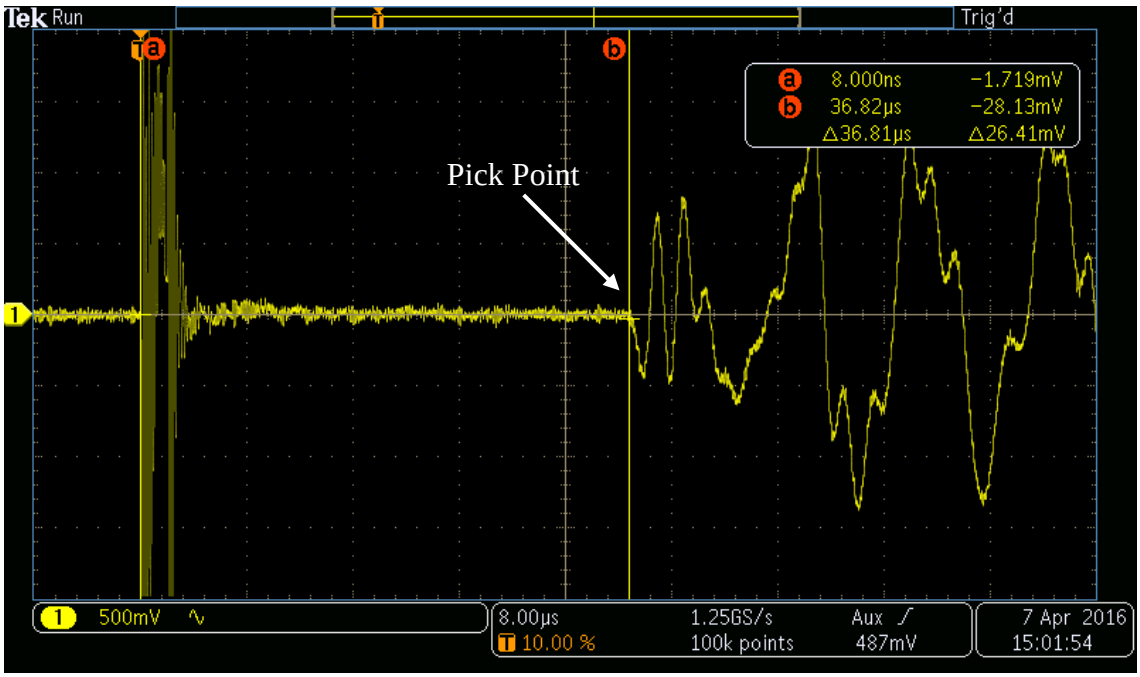

Figure 21. Screenshot of the oscilloscope measuring the P-wave travel time for sample A at 3500 psi confining pressure

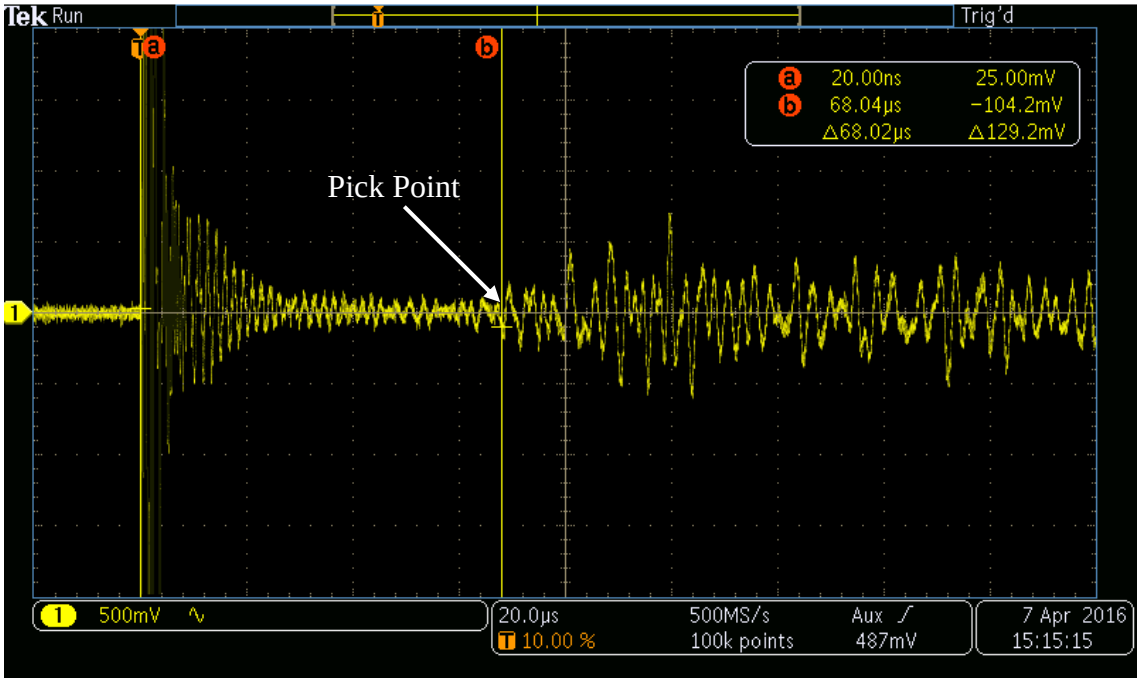

Figure 22. Screenshot of the oscilloscope measuring the S-wave travel time for sample A at 3500 psi confining pressure

Table 3. Sample A Velocity Measurements

Confining Pressure (psi)	DENSITY (g/cc)	P-wave velocity (m/s)	S-wave velocity (m/s)	Dynamic Elastic Modulus (GPa)	Dynamic Poisson's ratio
3500	2.64	4913.72	3073.29	58.71	0.18
0		4724.73	2963.64	54.45	0.18

Triaxial Testing and Injection

Two main objectives for this test were to conduct a triaxial-injection test to understand the rock response to stimulation. And to collect all possible geomechanical information from the sample. This includes Mohr-Coulomb envelope, sample compressive strength, elastic parameters etc.

Test Parameters are presented in the Table 4.

Table 4. Triaxial Test Input Parameters

Specimen Type	Basalt
Specimen Diameter	63.4 mm
Specimen Length	127.51 mm
Loading method used	Strain control
Strain Loading Rate	1x10-5 strain/sec
Effective Confining Pressure	1500-3500 psi (Multistage test)
Pore pressure differential across sample (Nitrogen)	300 psi
Strain measurements undertaken	One axial LVDT's, two strain gauges at center of sample – One axial and one radial

Test Results

A description of each of the tests conducted on the sample is shown below:

Room Temperature Test for Measurement of Elastic Parameters

Confining pressure was increased to 3500 psi at room temperature. Before beginning loading the sample, the piston was lowered to come into contact with the sample. This was done by changing the displacement with a rate of 0.1 mm/sec on the MTS software and watching the force reading on the monitor. Having the force reading change from zero to a positive number indicated that the sample is touched by the piston. The sample was then loaded to a differential stress of 45 MPa at a strain rate of $1x10^{-5}$ strains/sec. And then unloaded back.

Using the recorded data of the test, the differential stress is plotted versus axial strain. To calculate the average Young's modulus the slope of the initial linear part of the plot which is about first half of the plot from beginning to dilation point is calculated which is shown in Figure 23. Also the radial strain is plotted versus axial strain and the after adding a trend line, the slope of the trend line is calculated as the Poisson's ratio of the sample which is shown in Figure 24.

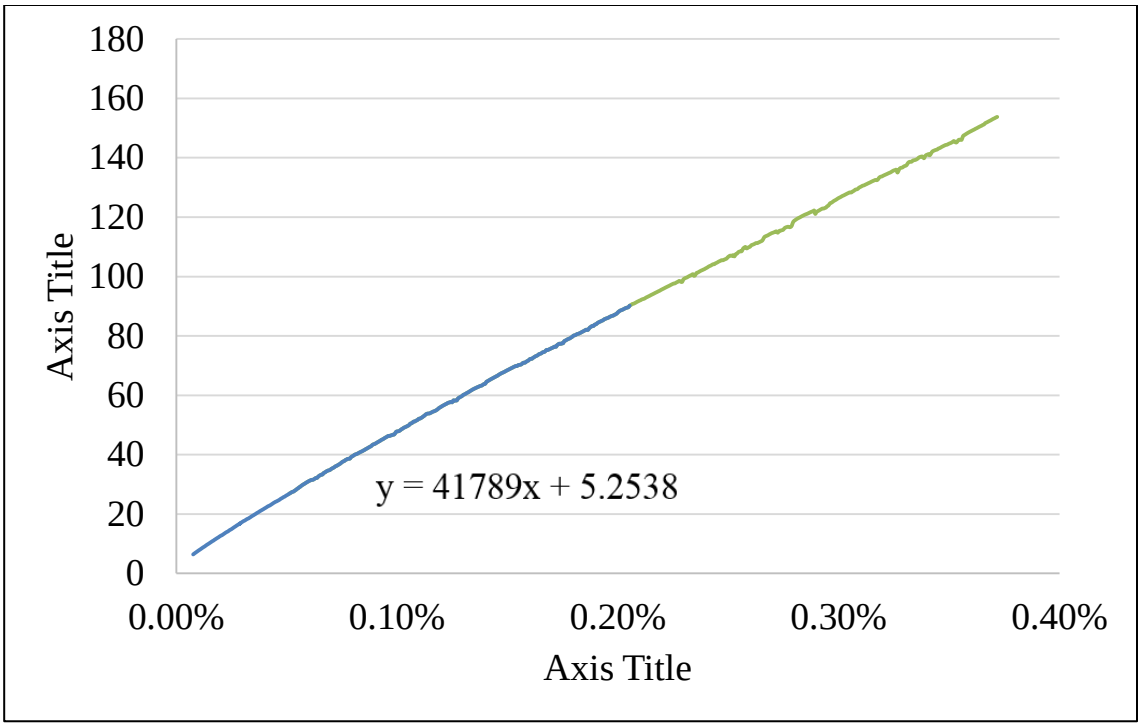

Figure 23. Stress vs Strain Plot for Sample A Conducted at 3500 psi Confining Pressure and Room Temperature for Young's Modulus Calculation

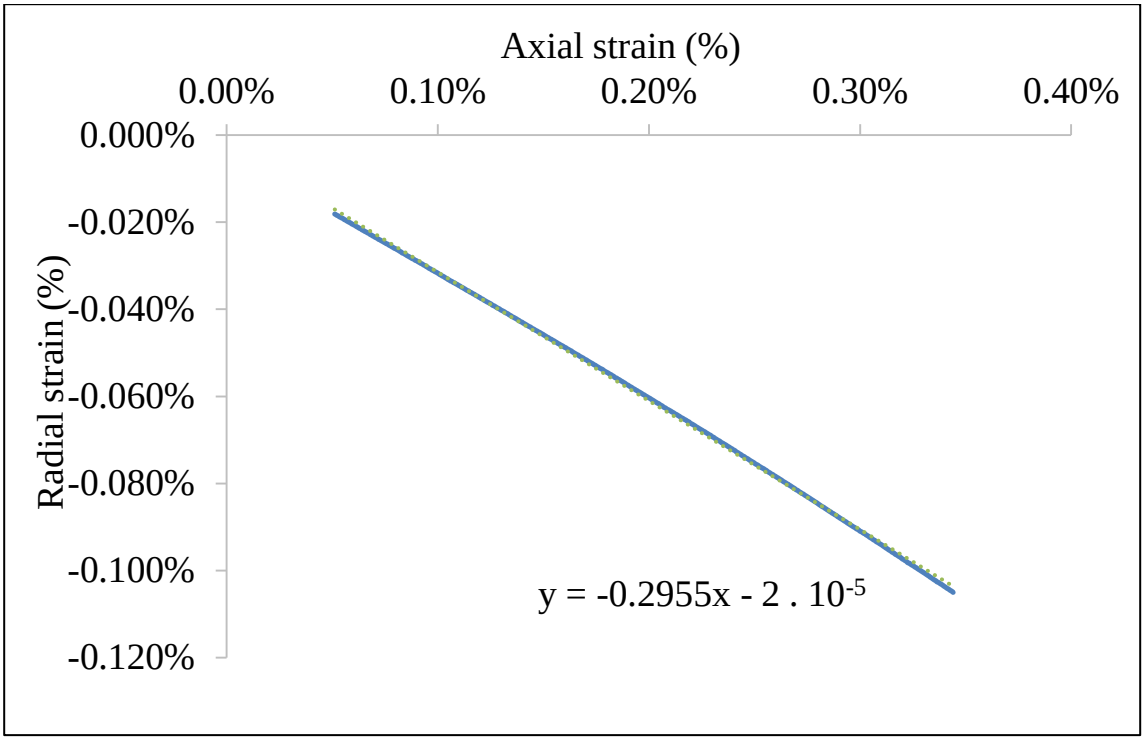

Figure 24. Radial Strain vs Axial Strain Plot for Sample A Conducted at 3500 psi Confining Pressure and Room Temperature for Poisson's Ratio Calculation

High Temperature Test

The sample was heated at a rate of 1.5ºC/min. Strains (axial and radial) were recorded using LVDT. The plot below shows the effect of heating on the strain (Figure 25)

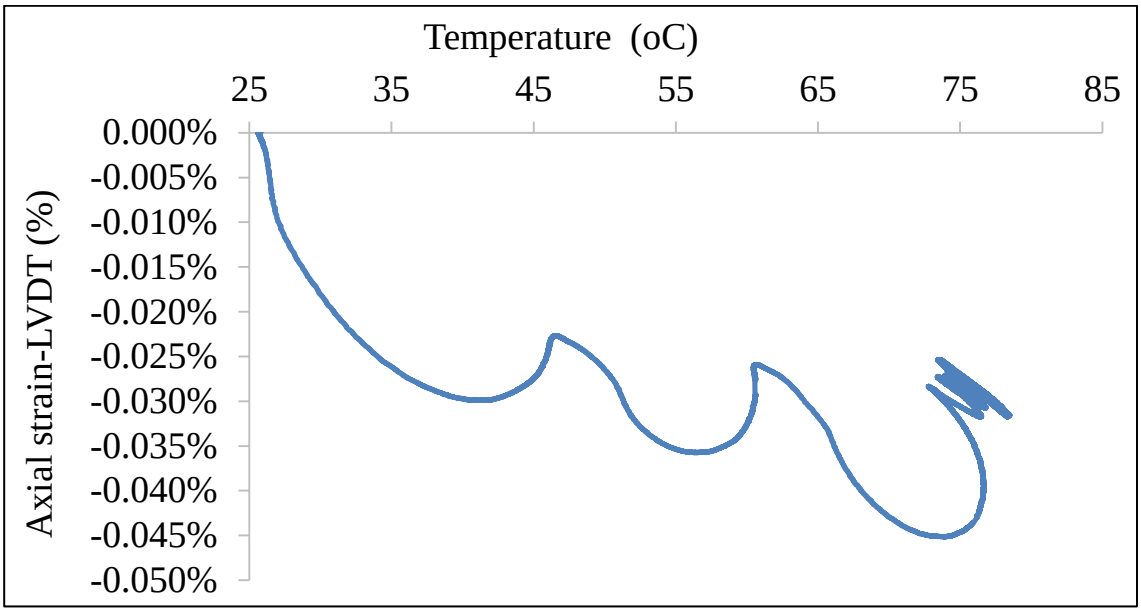

Figure 25. Effect of Heating on the Strain (Negative Signe Means Expansion)

As can be seen, the sample increases in length by almost 0.03% when the temperature is raised to 75 ºC from 25 ºC. In the end we can see some fluctuation in strain which is due to the temperature controller error in maintaining sample temperature; it still varies by +/- 5 ºC once stable. Another way to represent this is by using a time and temperature vs strain plot (Figure 26).

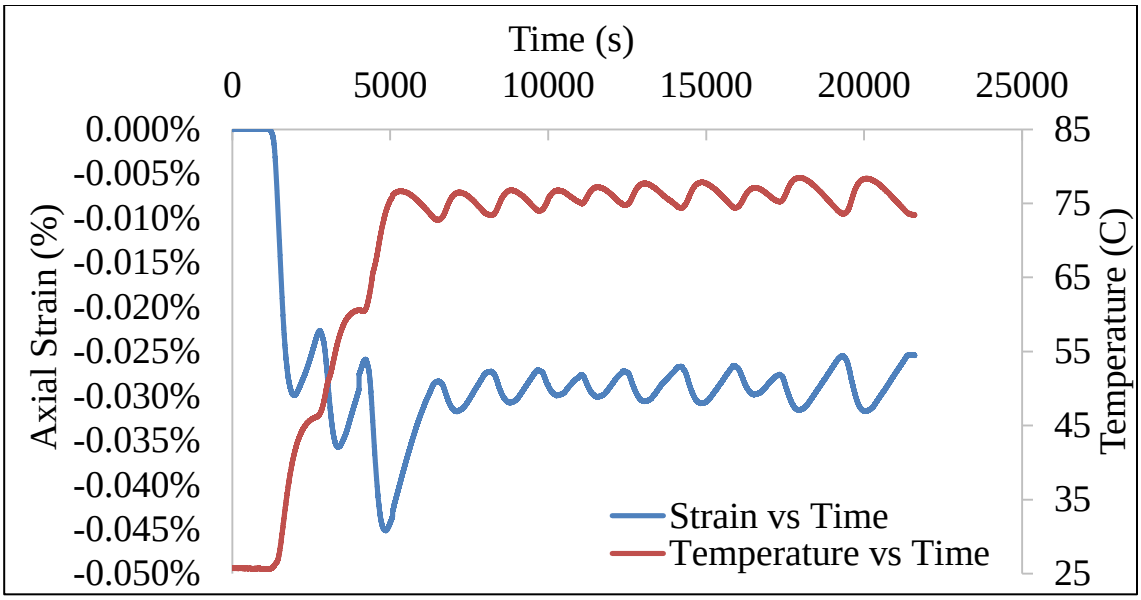

Figure 26. Time and Temperature vs Strain (Negative Signe Means Expansion)

This plot shows that temperature varies by +/- 5 ^{o}C which results in similar changes in strain.

Verifying if the sample will fail due to injection

This test was conducted to understand if a stimulation carried out by injection of gas into the sample resulting into an effective confining pressure of 1000 psi (from the initial 3500 psi) would be successful. The sample was therefore subjected to estimate in-situ conditions of 10000 psi vertical stress and 3500 psi horizontal stress. The sample was axially loaded to a vertical stress of 10000 psi at a strain rate of $1x10^{-5}$ strains/sec while maintaining a confining pressure of 5500 psi (Not effective) and a temperature of 90 ^{o}C. Then vertical stress was maintained constant at 10000 psi, while nitrogen gas was injected at a pressure of 2000 psi resulting into an effective confining pressure of 3500 psi. The injection was maintained for 30 mins from both ends of the sample to reach desired pore pressure faster. After 30 minutes the flow rate on both injection pumps to the top and bottom of the sample reached an equal flow rate with opposite

sign which indicated a uniform pore pressure in the sample. However, sample didn't fail. This answered one desired question for testing of this sample, that sample won't fail due to a stimulation treatment with an effective confining pressure of 3500 psi (assuming a vertical differential stress of 10000psi). Then the pore pressure increased to 4500 psi resulting in an effective confining pressure of 1000 psi. However the sample still did not fail due to injection. Since the intention of the test was to create the Mohr - Coulomb envelope by performing a multistage triaxial test I did not increase the deviatoric stress to fracture the sample.

Multistage Triaxial testing

A multistage triaxial testing program was conducted to construct a Mohr circle failure envelope for the sample. The sample was tested at effective confining pressures of 3500 psi, 2000 psi and 1500 psi. It was failed at 1500 psi effective confining pressure. Figures 27 and 28 show the stress vs strain plots and the Mohr - Coulomb envelope constructed for Sample A. The point at which deflection in volumetric strain occurred was taken as the failure strength for each confining pressure of 3500 psi, 2000 psi and 1500 psi to find the failure envelope on the Mohr Coulomb plot. Failing the sample at 1500 psi gave the real strength of the sample for that confining pressure, which leads to generate the actual envelope as presented in Figure 28. Figures 29 and 30 show the stress vs strain plot presenting the Young's Modulus and radial strain vs axial strain plot showing Poisson's ratio for Sample A. The parameters resulted from stress strain plots and the Mohr - Coulomb envelope are presented in Table 5.

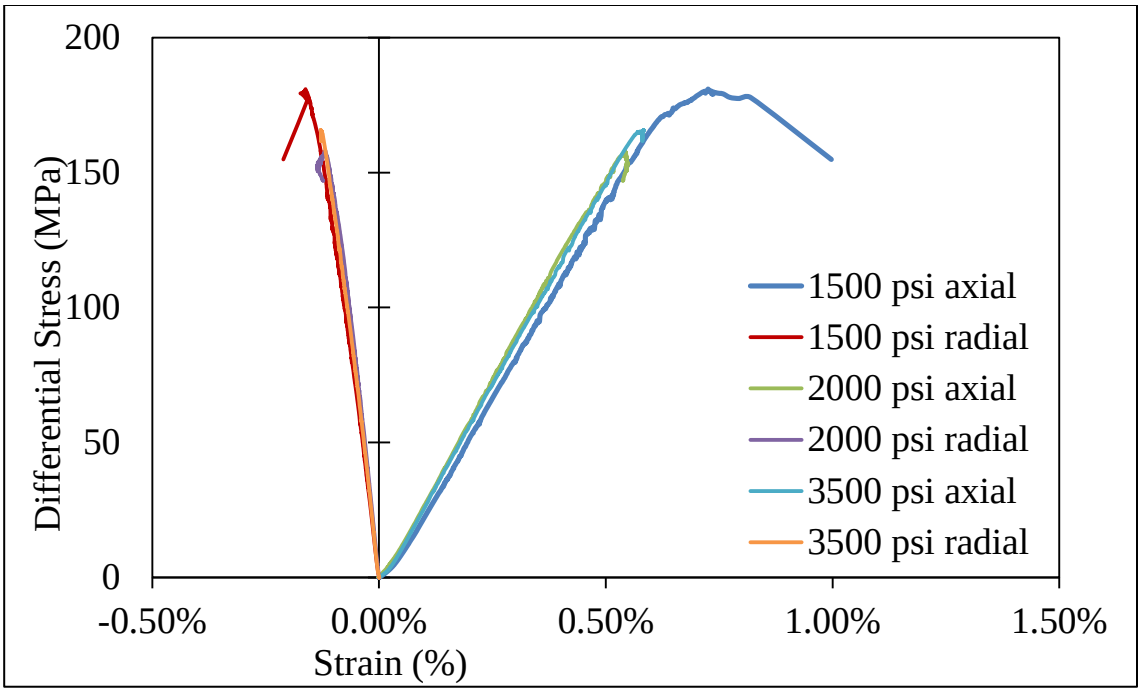

Figure 27. Differential Stress vs Strain Plot for Sample A

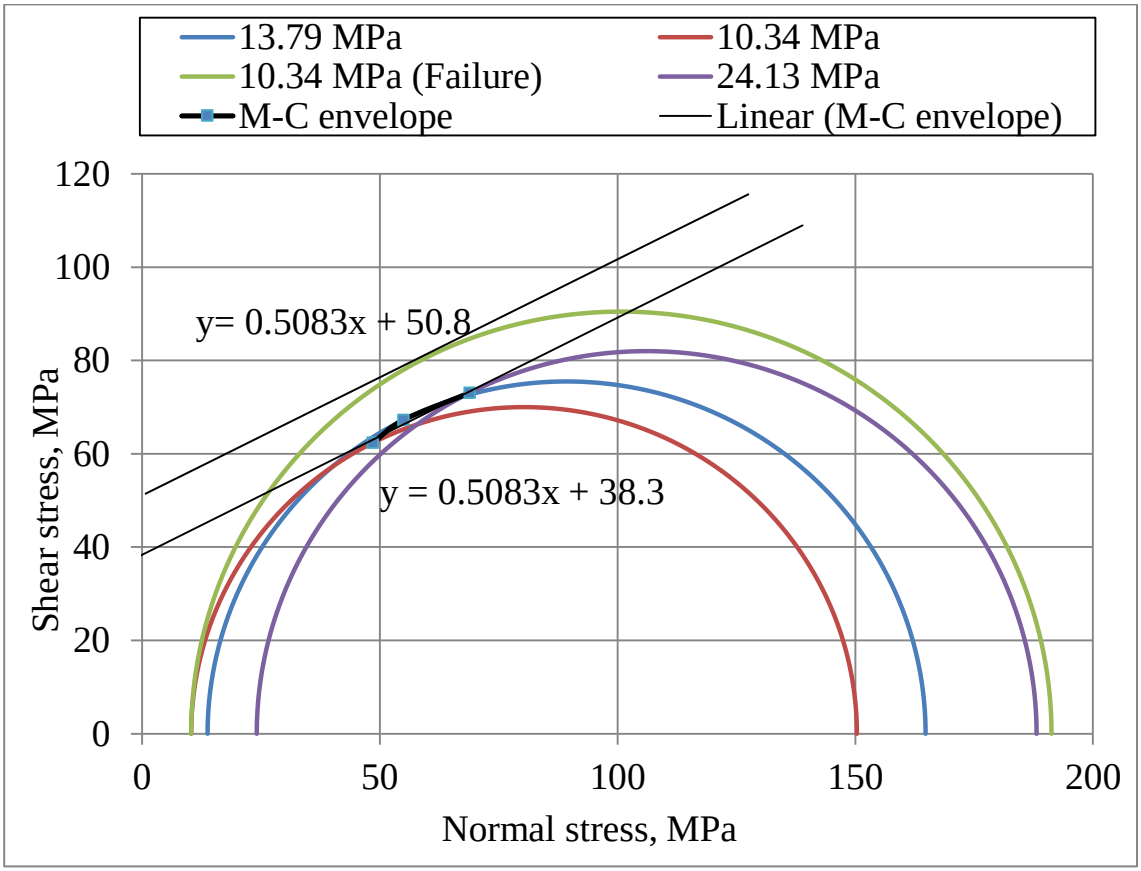

Figure 28. Mohr - Coulomb Envelope Plot for Sample A

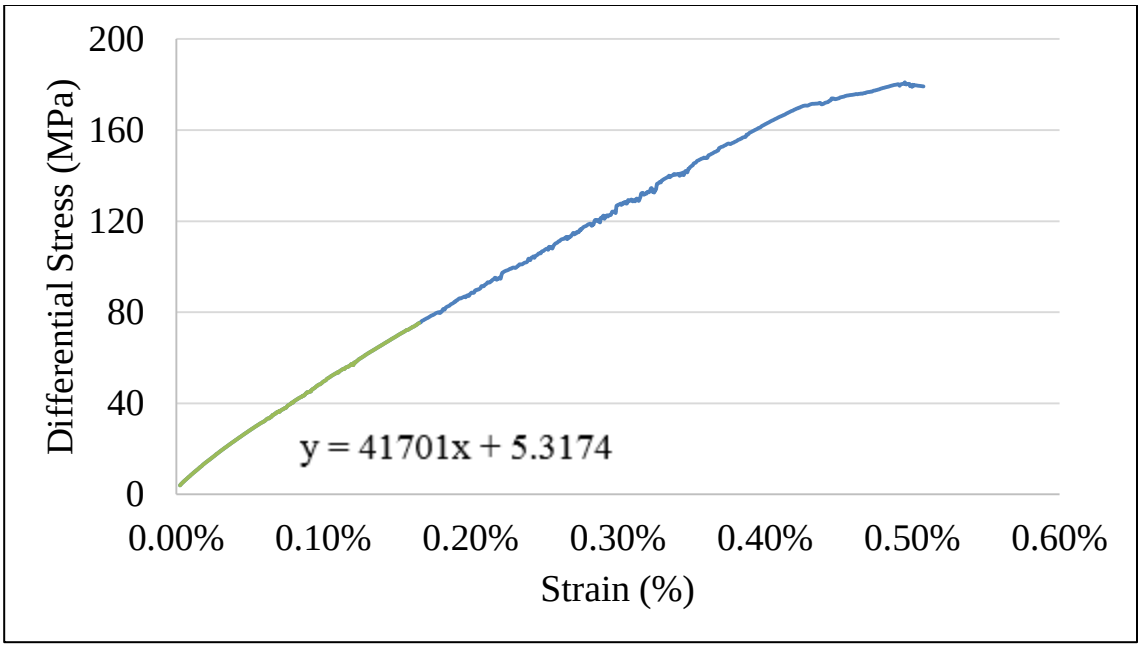

Figure 29. Stress vs Strain Plot Presenting the Young's Modulus for Sample A at High Temperature equals 41.7 GPa

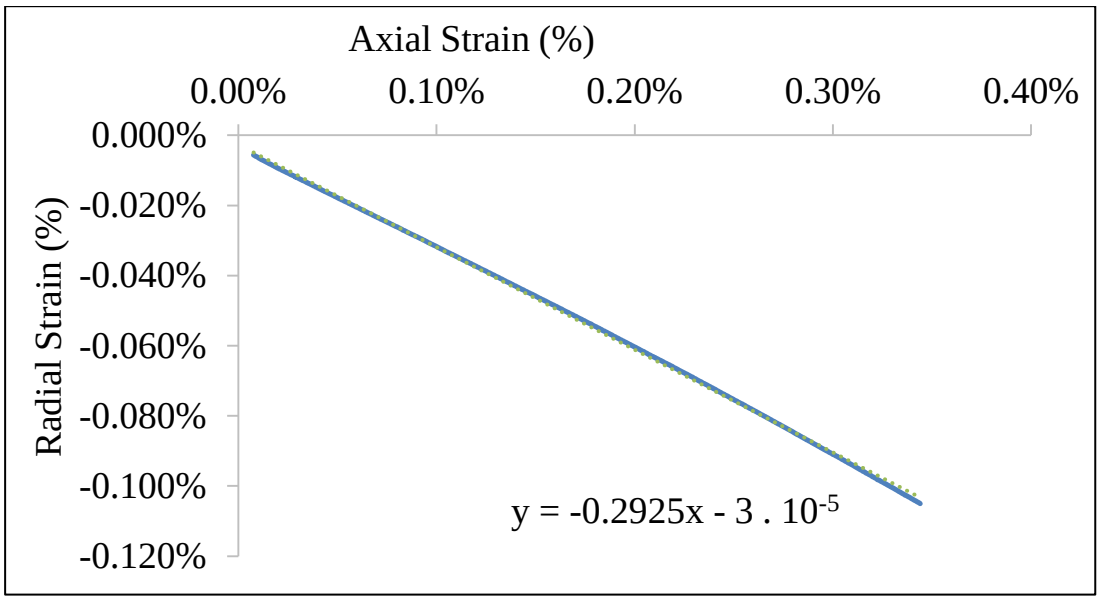

Figure 30. Radial Strain vs Axial Strain Plot Showing Poisson's Ratio for Sample A at High Temperature equals 0.29.

Table 5. Results from Stress vs Strain Plots and The Mohr - Coulomb Envelope

Average Young's Modulus*	41.7 GPa
Average Poisson's ratio*	0.29
Peak Strength**	180.9 MPa
Axial strain at failure**	0.66%
Initial Permeability*	46.8 nD
Angle of friction	26.9^{O}
Cohesion	50.8

* Both at effective confining pressure of 3500 psi
** At effective confining pressure of 1500 psi

Permeability was measured after failure the same way it was measured before fracturing. Top and bottom of the sample each were connected to a separate syringe pump. The pump connected to the top of the sample was injecting with a pressure of 2000 psi and the pump connected to the bottom of the sample was injecting with a pressure of 1900 psi. Until the flow rate got stable on both pumps and the gas was getting injected and received at a same flow rate. At this point the flow rate was recorded and having dimensions of the sample the permeability was calculated using Darcy's law. The permeability showed a large increase from 46.8 nD to >500 µD reflecting an increase of more than 1000 times (zero differential pressure, confining pressure of 3500 psi). The increase can be attributed to the large fracture seen to cut through the sample's end after failure. It should be noted that there were multiple fractures with one large axial and an inclined large fracture (Figure 31).

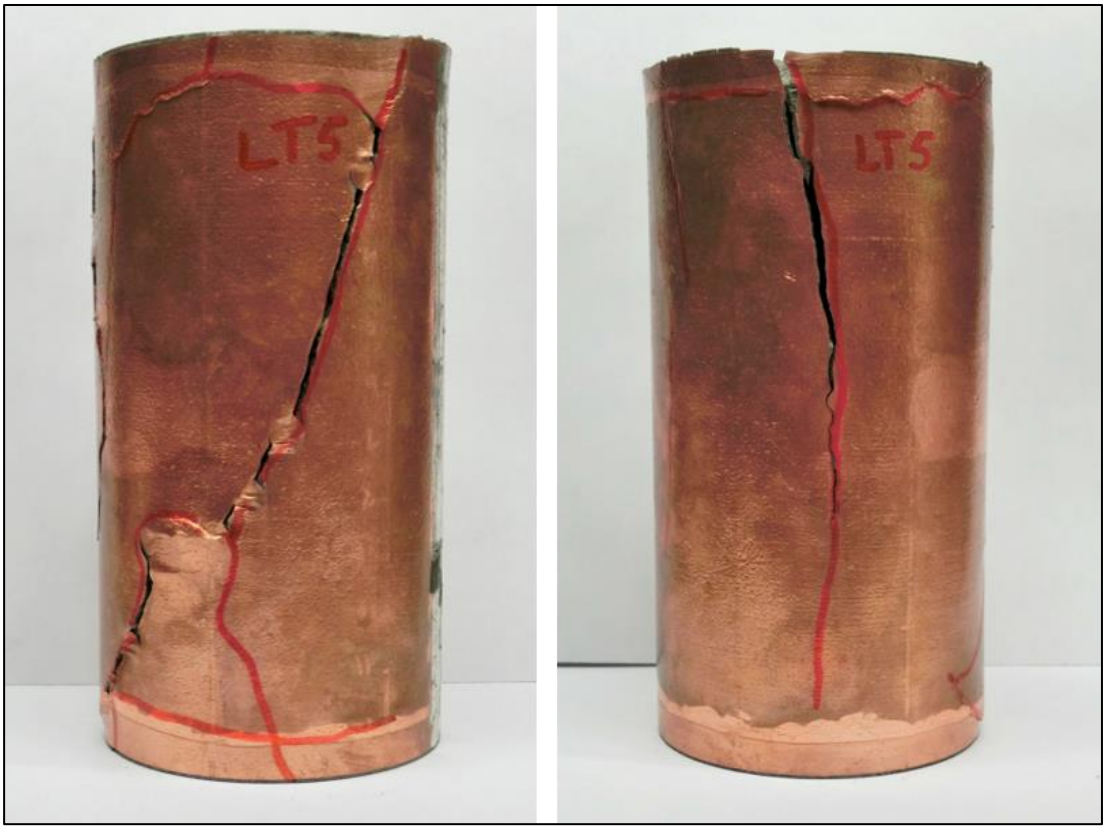

Figure 31. Sample A after Failure (Two Views)

Acoustic Emissions analysis

Eight crystals placed across the sample as explained in Chapter 2 (Figure 32). A droplet of the "E-Z bound instant glue thick" with viscosity of 1500 CPS applied to the face of each AE crystal and then the crystals were placed on the sample surface by pushing it to the sample surface with fingers and holding it for 30 seconds to have it attached to the sample surface well. The amplitude cut off for all tests conducted on this sample was 60dB. The higher amplitude cut off for this test can be attributed to the use of frame MTS 816 which has less noise cancelling capability than the larger and better sound insulated frame MTS 315. More detail on Acoustic Emission threshold amplitude determination and noise reduction is explained in appendix B.

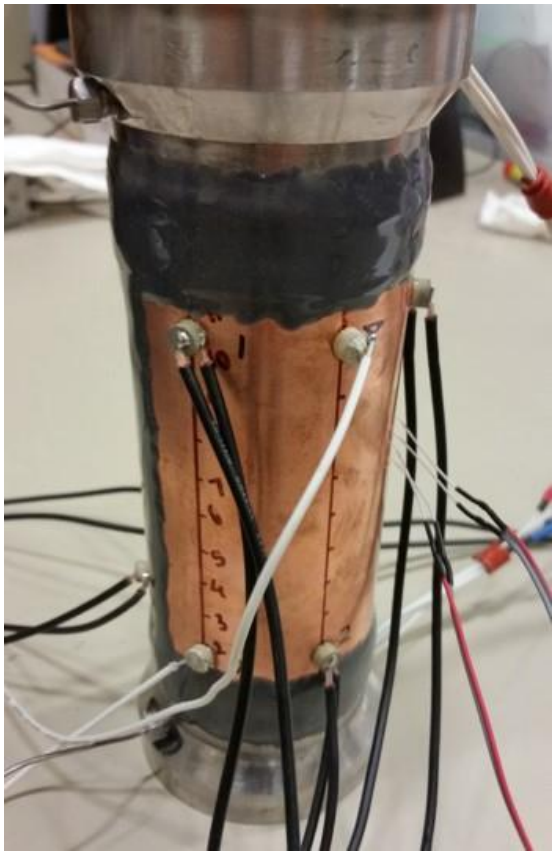

Figure 32. Sample A with Attached Acoustic Emission Crystals

The following Figures 33 and 34 show the results of the Acoustic emissions for the triaxial test with confining pressure 1500 psi, the final triaxial test which resulted in sample failure. As can be seen, most of the AE events are generated during failure due to the formation of fracture as expected.

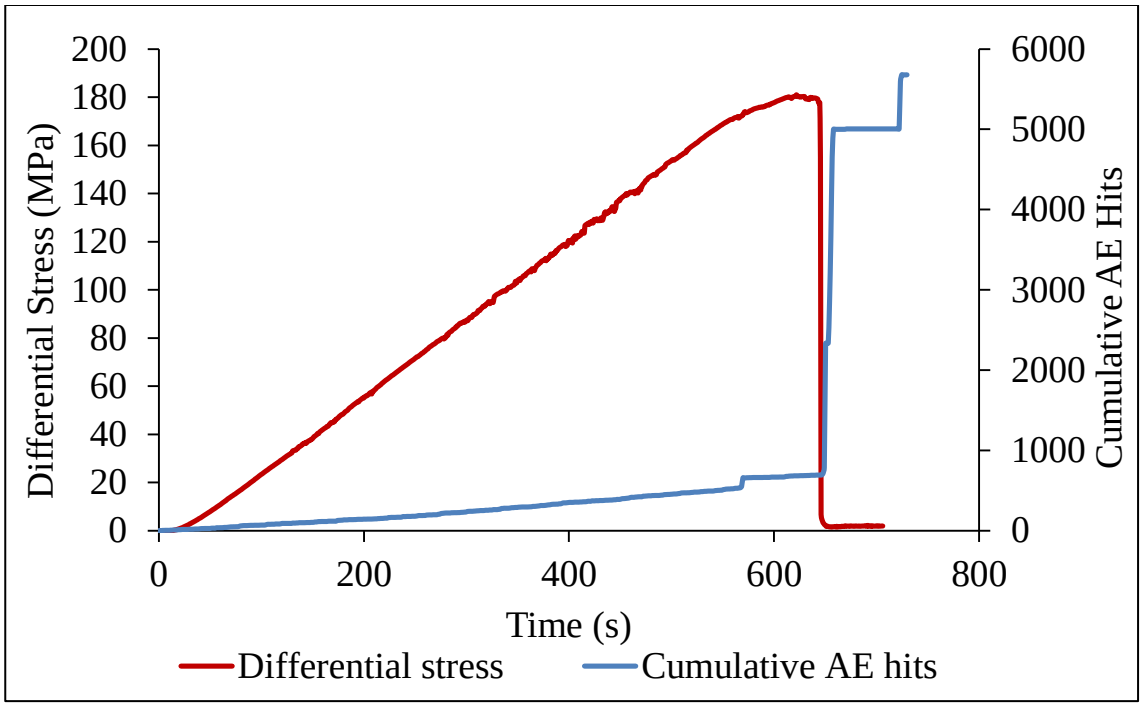

Figure 33. Differential Stress and Cumulative AE Hits vs Time for Sample A

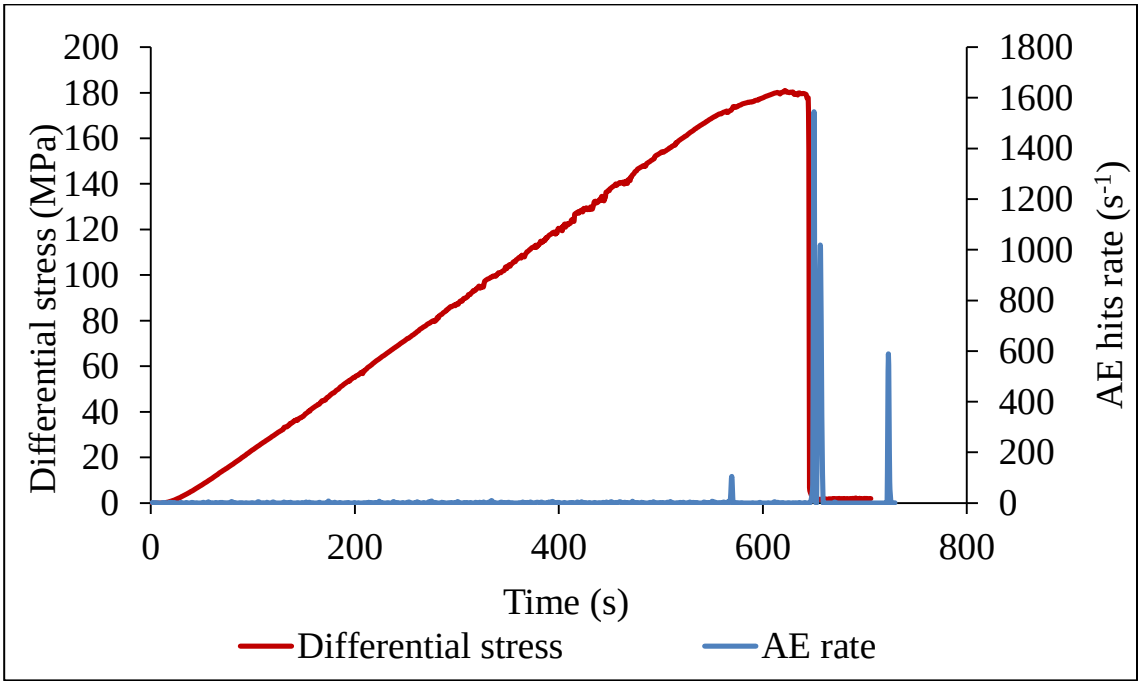

Figure 34. Differential Stress and AE Hits Rate vs Time for Sample A

The location of these events was done in 2-D as well as 3-D using MISTRAS software. This is shown in Figure 35 and 36 below. The location of events can be seen to match reasonably with the actual fracture, although location algorithm also picks up some micro-cracking events within the sample at locations further away from the fracture.

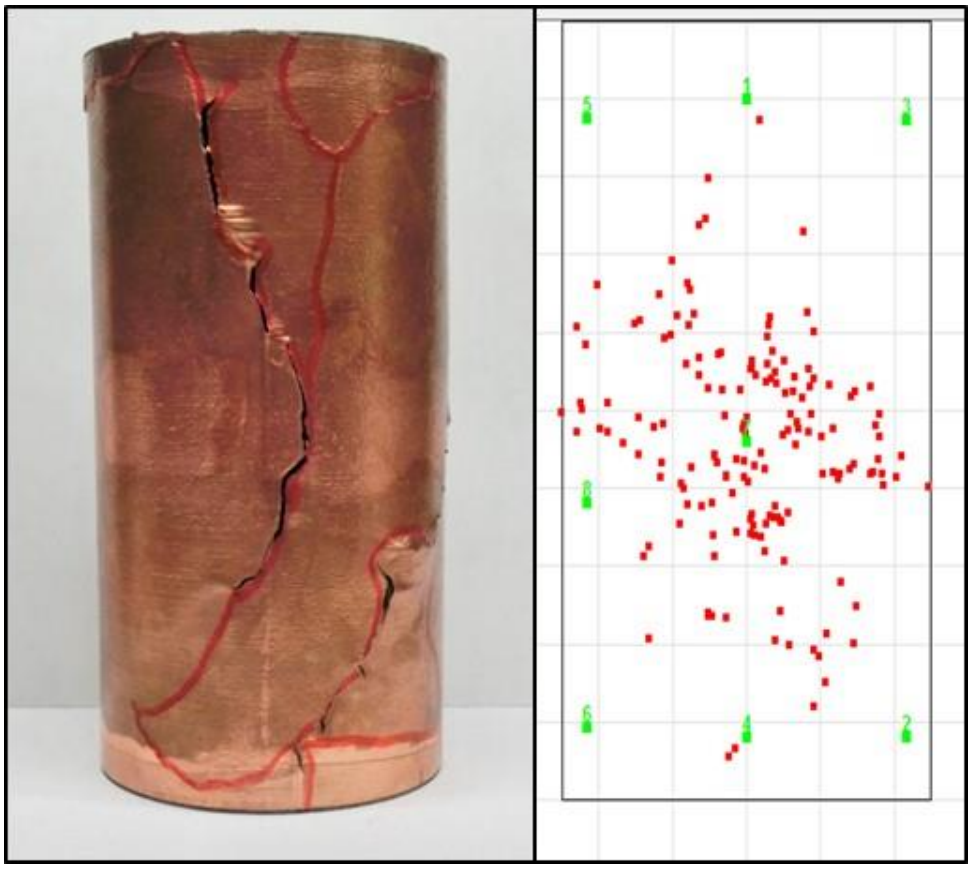

Figure 35. The Location of the Events Presented in 2-D Using MISTRAS Software beside the Fractured Sample A

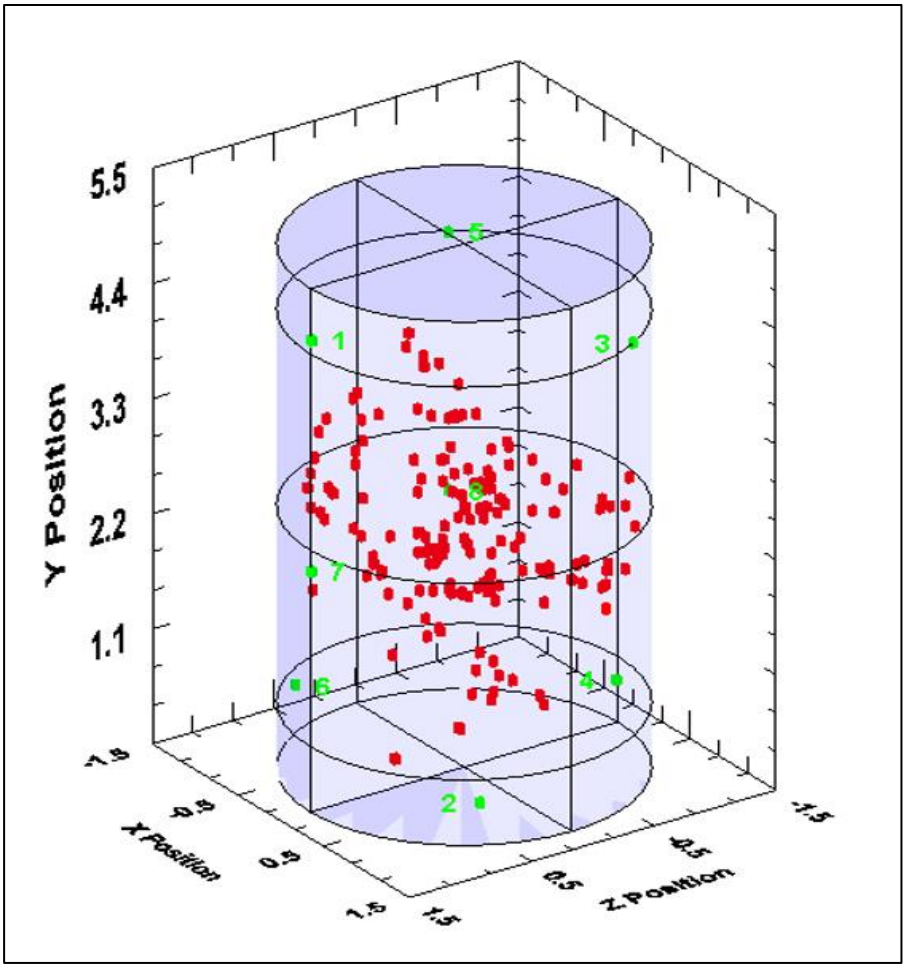

Figure 36. The Location of the Events Presented in 3-D Using MISTRAS Software for Sample A

We can see from the plots that the AE is mainly generated in the location of the fracture. The generated 3-D location is not completely accurate since it fails to pick up more events closer to the ends because both heads of the sample are covered with epoxy and it is not possible to attach the AE crystals at the tip of the sample but the closest place on the sample not covered with epoxy.

Chapter 5: Sample B - Tests, Procedures and Results

Sample Description

The sample is purplish in color and has an average depth of 4242.5 ft (uncut core depth of 4239.5 – 4245.5 ft). It has a length of 122.4 mm (4.8 in) and 63.5 mm (2.5 in) in diameter (L/D ratio of 1.9:1). The sample has white calcite veins (confirmed by XRD) running across the sample (Figure 37). It shows no visible fractures, minor or major. It does show few white and colored inclusions which vary in size from <1 mm – 5mm in length (Figure 38). Grain structure is fine grained and very well consolidated. Its mineral content is covered in the next section.

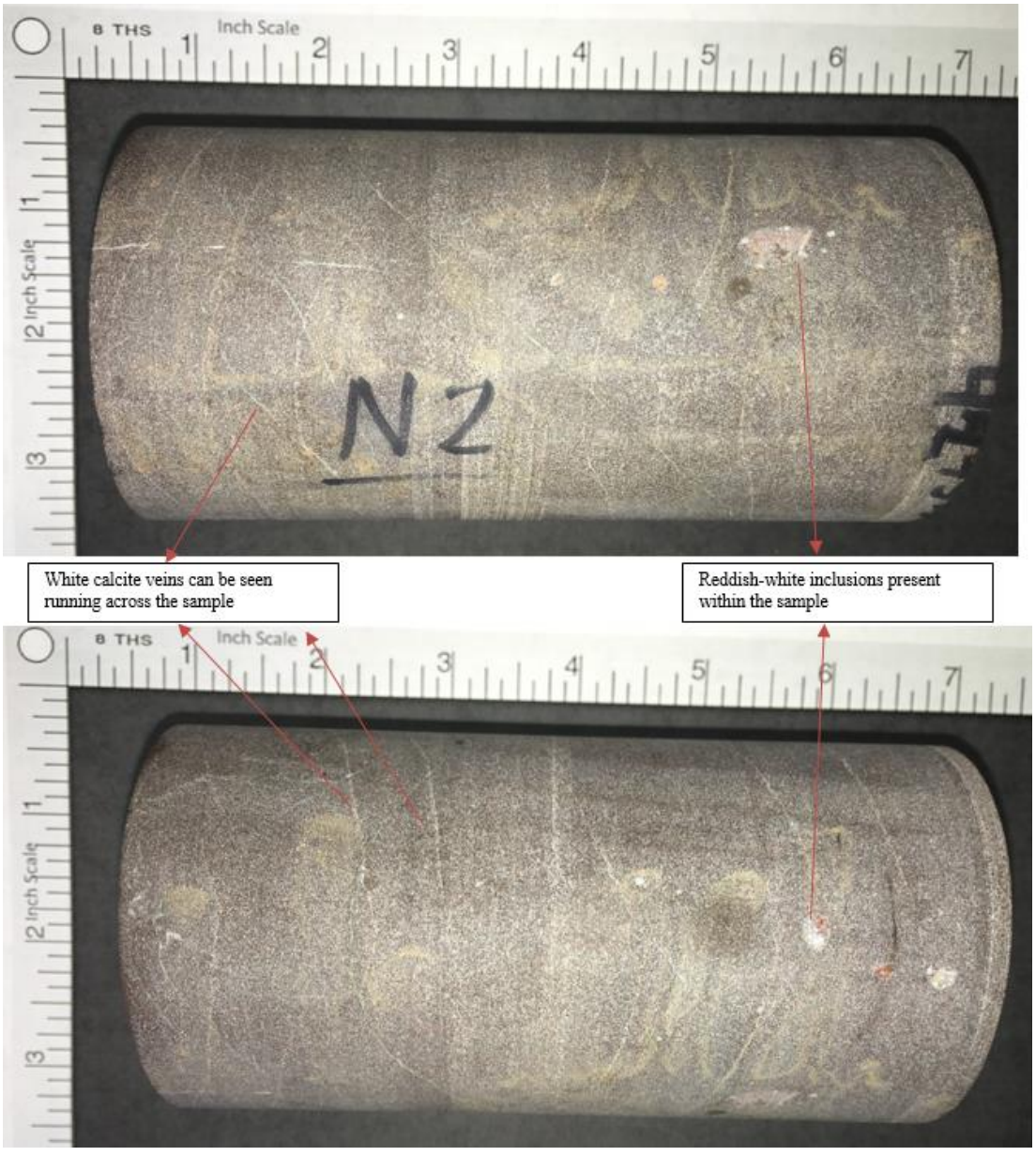

Figure 37. Sample B Cut and Polished Before Test

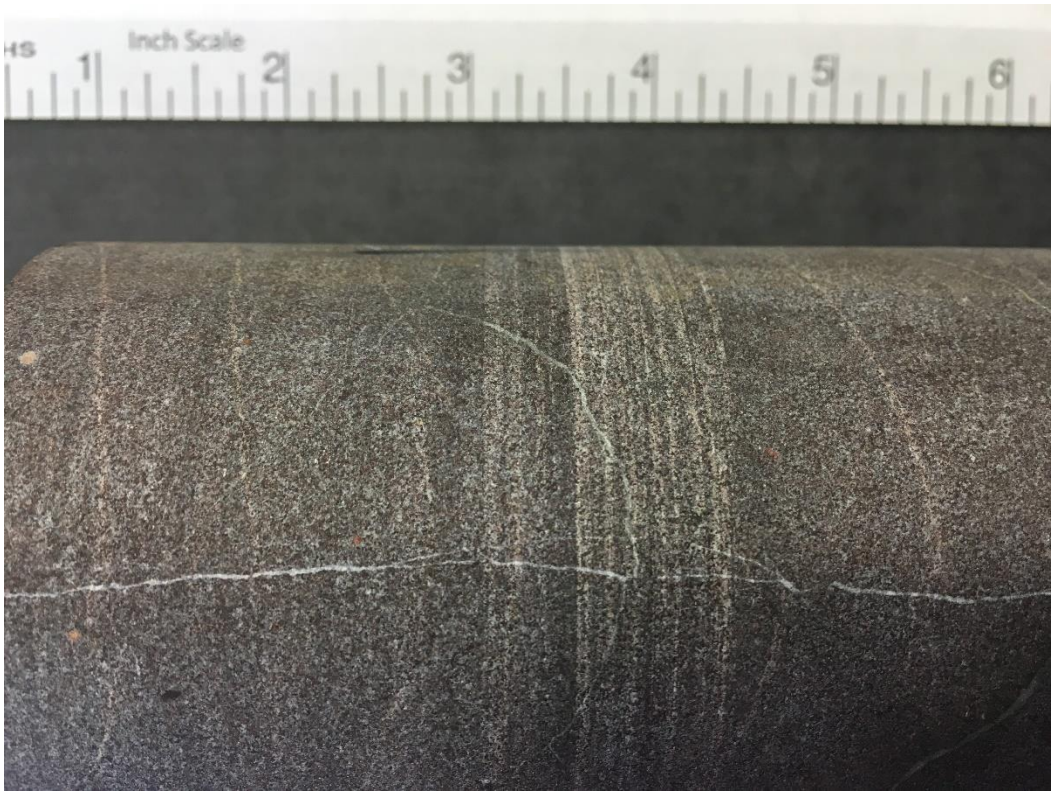

Figure 38. Zoomed in Version of Sample Showing the Calcitic Veins Present in the Sample Clearly

XRD Results

Same as previous sample the mineral content of this sample is determined by XRD test. Table 6 shows the mineral content of sample B.

Table 6. Mineral content in Sample B

Minerals	Weight (%)
Albite	33.1
Labradorite	42.1
Vermiculite	15
Quartz	6.6
Hematite	3.2

Comparing the mineral contents of the sample A and sample B shows both of them contains Albite and Quarts and at about the same percentage, however the other minerals are different between two samples.

Dynamic Velocity measurements

Dynamic velocity tests were carried out with axially placed compressional and shear crystals of frequency 500 Hz. Measurements were carried out at the desired final confining pressure (3500 psi). Appendix A explains how to measure the dynamic velocity. Figure 39 and Figure 40 show a screenshot of the oscilloscope measuring the P-wave and S-wave travel time for sample B at 3500 psi confining pressure. Results are summarized in Table 7.

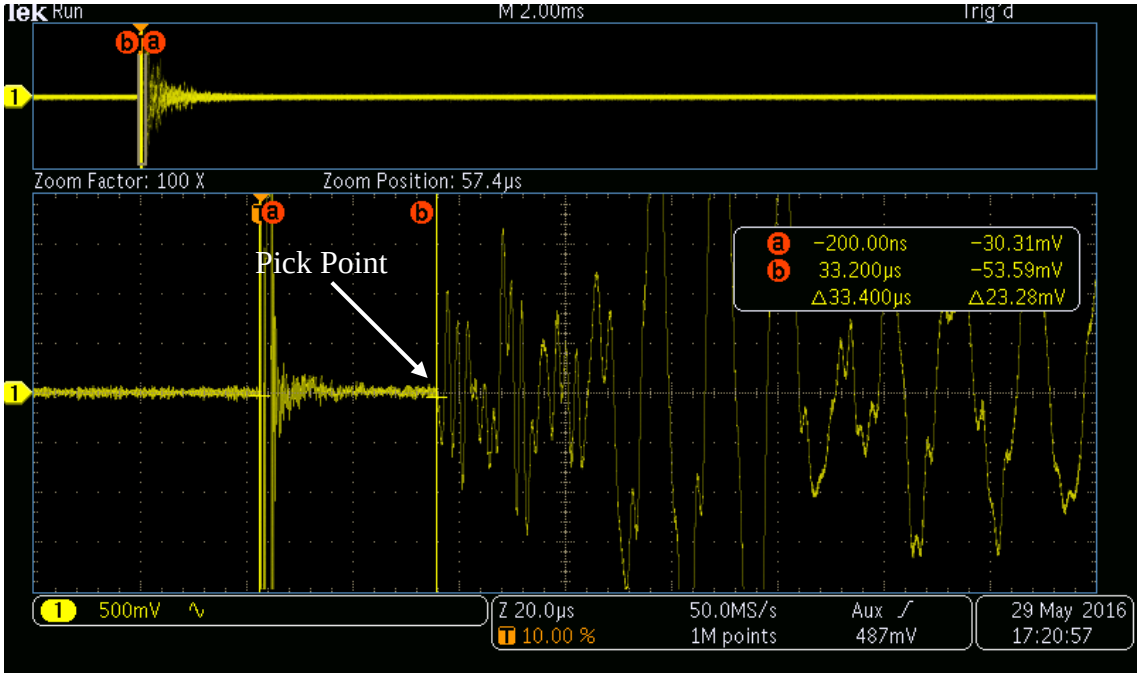

Figure 39. Screenshot of the oscilloscope measuring the P-wave travel time for sample B at 3500 psi confining pressure

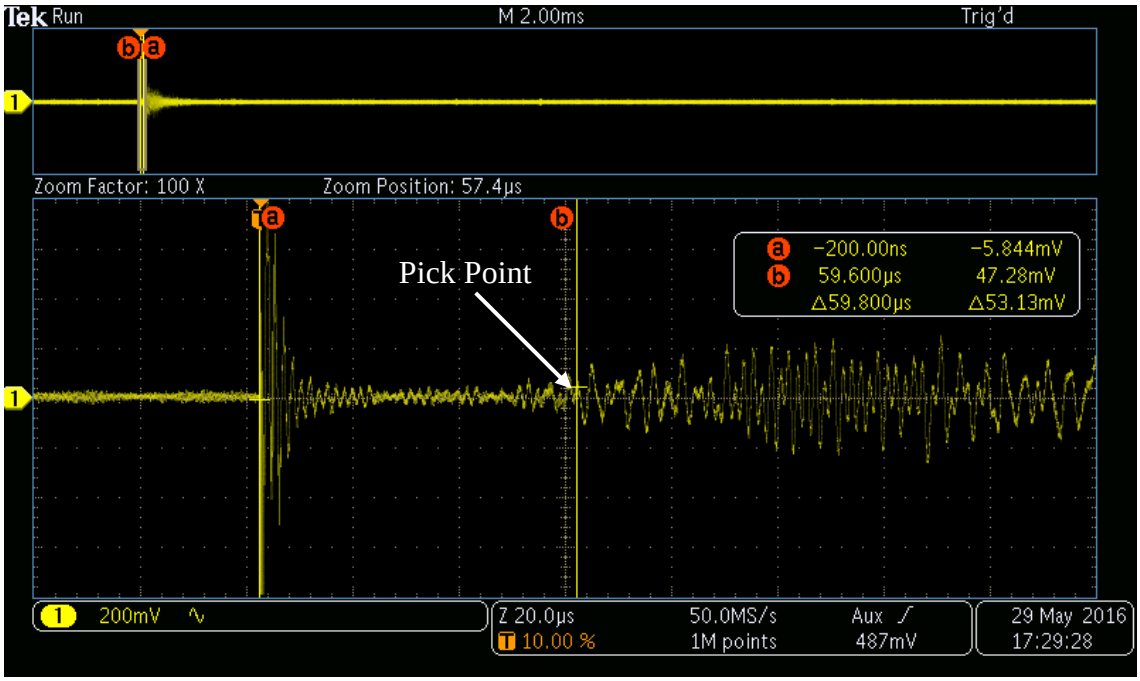

Figure 40. Screenshot of the oscilloscope measuring the S-wave travel time for sample B at 3500 psi confining pressure

Table 7. Sample B Velocity Measurements

Sample Designation	DENSITY (g/cm^3)	P-wave velocity (m/s)	S-wave velocity (m/s)	Dynamic Elastic Modulus (GPa)	Dynamic Poisson's ratio
Sample B	2.74	5456.98	3285.91	71.83	0.22

Comparing the dynamic elastic modulus and dynamic Poisson's ratio calculated from the dynamic velocity measurements shows that sample A has about 22% higher dynamic elastic modulus and dynamic Poisson's ratio than sample B.

Triaxial testing and Injection

Testing sample B has the same objectives as sample A. The main objective is to have a successful triaxial-injection test in mentioned conditions.

Test parameters for sample B are presented in the Table 8.

Table 8. Triaxial Test Input Parameters

Specimen Type	Basalt
Specimen Diameter	63.5 mm
Specimen Length	122.4 mm
Loading method used	Strain control
Strain Loading Rate	1x10-5 strain/sec
Effective Confining Pressure	1500-4500 psi (Multistage test)
Pore pressure differential across sample (Nitrogen)	200 psi
Strain measurements undertaken	One axial LVDT's, two strain gauges at center of sample – One axial and one radial

Testing Results

A description of each of the tests conducted on the sample is shown below:

Room temperature test for measurement of elastic parameters

Confining pressure was increased to 3500 psi at room temperature. The sample was then loaded to a differential stress of 45 MPa at a strain rate of $1x10^{-5}$ strains/sec. and then unloaded back. Using the recorded data of the test, the differential stress is plotted versus axial strain and after adding a trend line, the slope of the trend line is calculated as the average Young's modulus of the sample which is shown in Figure 41. Also the radial strain is plotted versus axial strain and the after adding a trend line, the slope of the trend line is calculated as the Poisson's ratio of the sample which is shown in Figure 42.

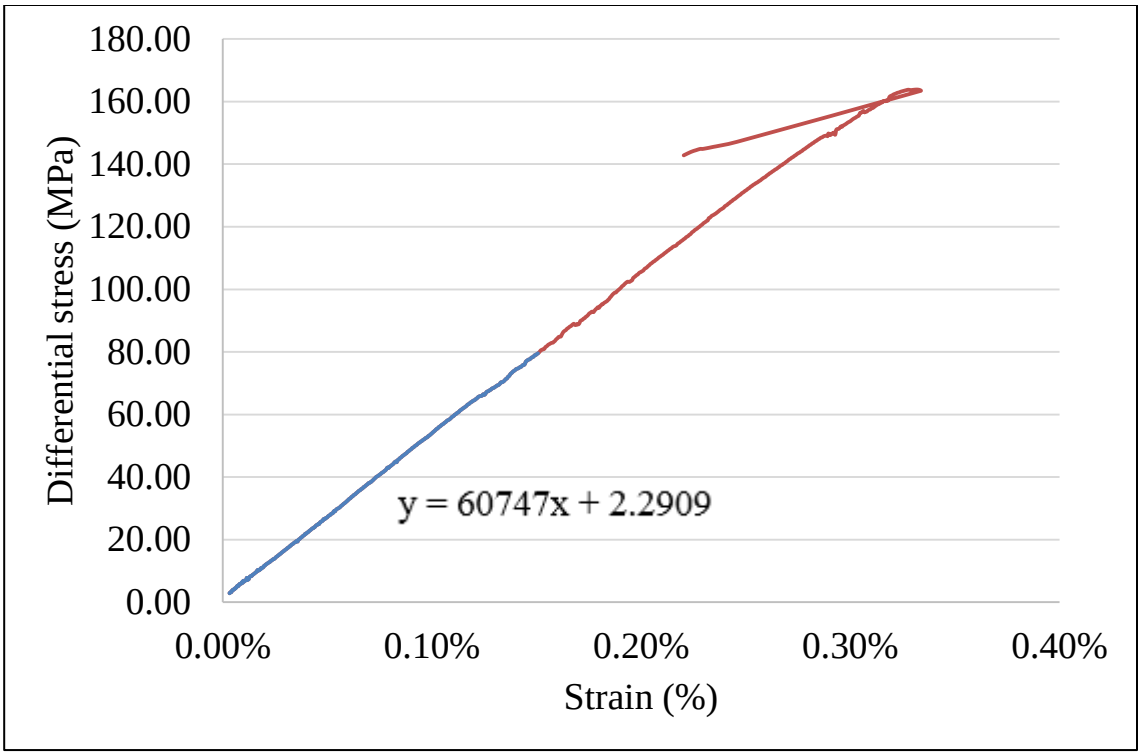

Figure 41. Stress vs Strain Plot for Sample B Conducted at 3500 psi Confining Pressure and Room Temperature for Young's Modulus Calculation.

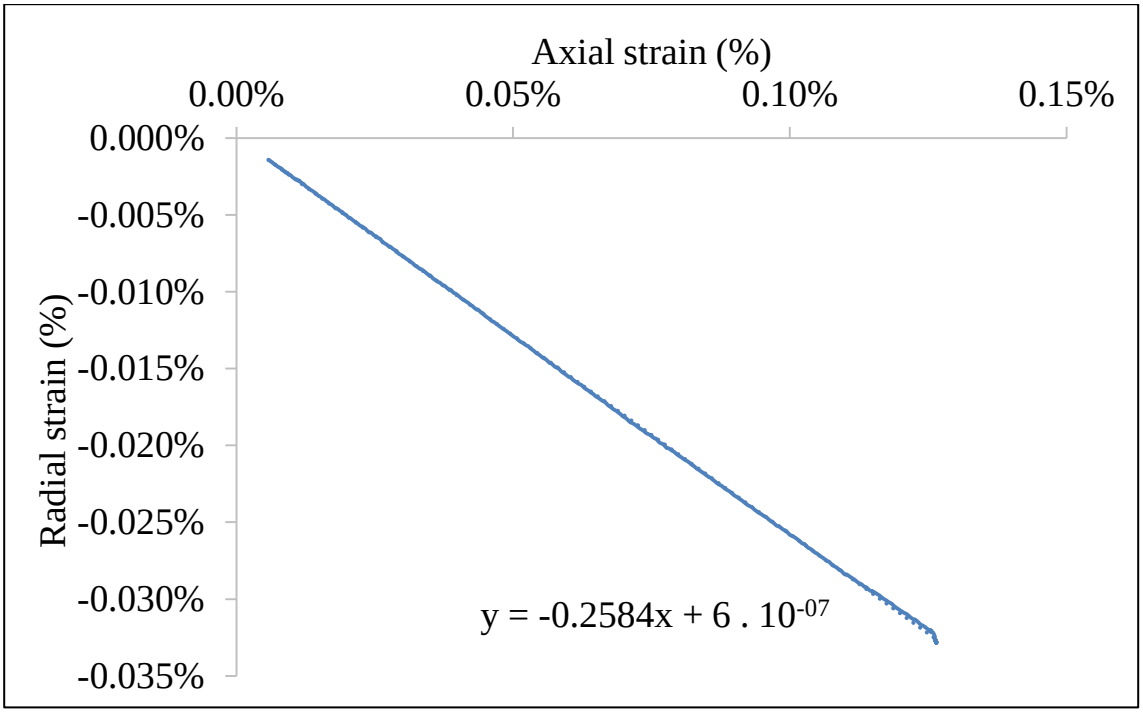

Figure 42. Radial Strain vs Axial Strain Plot for Sample B Conducted at 3500 psi Confining Pressure and Room Temperature for Poisson's Ratio Calculation.

Heating up the sample

The sample was heated at a rate of 1.5ºC/min. Axial strain was recorded using LVDT to quantify the length change of the sample. The plot below shows the effect of heating on the strain (Figure 43)

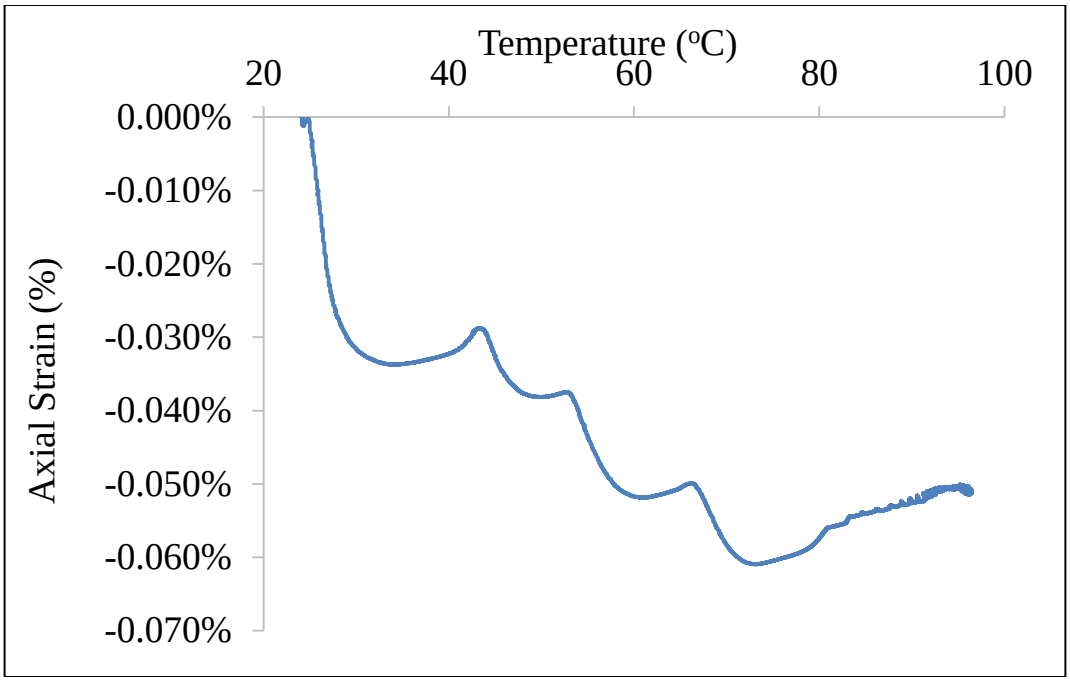

Figure 43. Effect of Heating on the Strain (Negative Signe Means Expansion)

Figure 44. Time and Temperature vs Strain

As can be seen, the sample increases in length by almost 0.03% when the temperature is raised to 75 ºC from 25 ºC. In the end we can see some fluctuation in strain which is due to the temperature controller error in maintaining sample temperature; it still varies by +/- 5 ºC once stable.

We can clearly see that the strain stabilizes after a few hours and then just shows normal hydrostatic creep.

Verifying the sample will fail due to injection

The triaxial-injection test performed on sample B same as sample A with the same procedure and configurations. Sample B did not fracture through the triaxial-injection test. Therefore the sample was loaded axially to near dilation point (turning point of the volumetric strain curve) and was then taken to failure by injection with the flow rate of 50 ml/sec.

Triaxial-Injection test at high temperature conditions

For the last part of the test, the intention was to fail the rock with injection. Therefore, at the moment of the turning point on the volumetric strain curve, the axial load was held constant and the sample was fractured by injecting nitrogen gas in to it. The sample temperature was 90^{o} C. Figure below shows the stress-strain plot for the test (Figure 45).

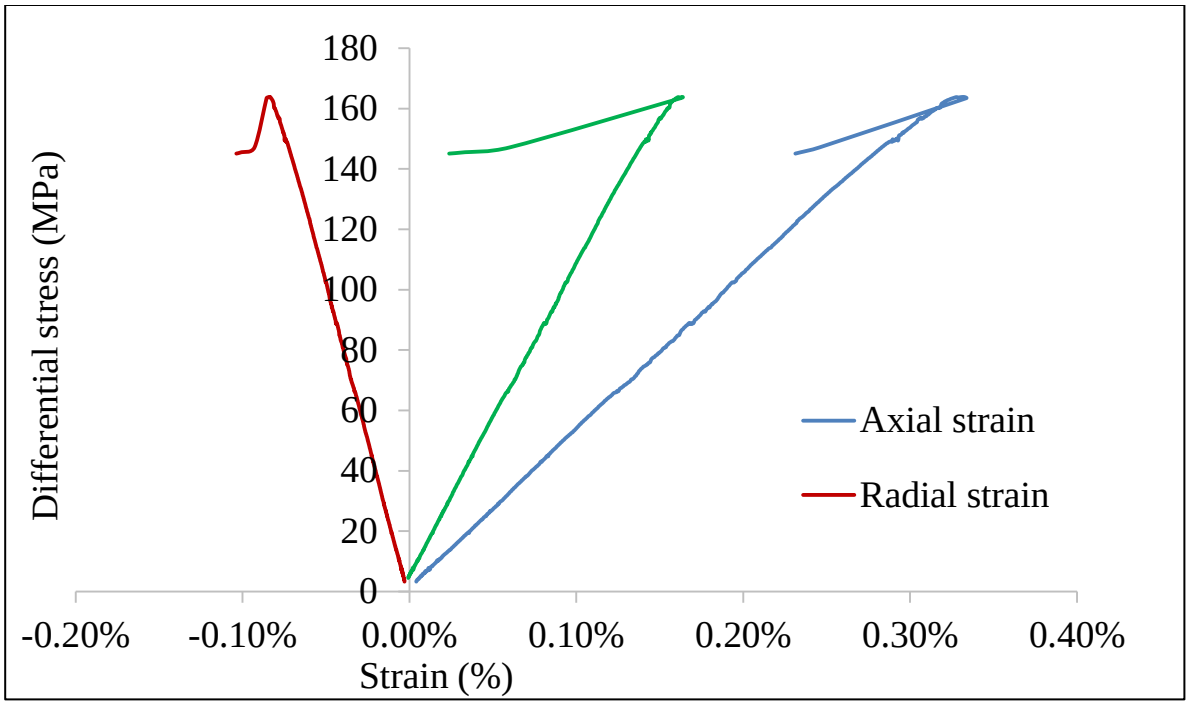

Figure 45. Differential Stress vs Strain Plot for Sample. All strains measured using strain gauges

Table 9. Results from Stress vs Strain Plots

Average Young's Modulus*	60.7 GPa
Average Poisson's ratio*	0.25
Peak Strength**	163.8 MPa
Axial strain at failure**	0.33%
Initial Permeability*	1.12 µD (micro Darcy)
Final Permeability*	10.2 µD (micro Darcy)

* At effective confining pressure of 3500 psi
** At effective confining pressure of 2500 psi

Permeability was measured after failure. The permeability showed a large increase from 1.12 µD to 10.2 µD reflecting an increase of about 10 times (no differential pressure,

confining pressure 3500 psi). The increase can be attributed to the large fracture seen in the sample after testing. It should be noted that there were multiple fractures with one large axial and an inclined large fracture which did not intersect the ends of the sample (Figure 46).

Figure 46. Sample B after Failure (Two Views)

Acoustic Emissions analysis

Eight crystals placed across the sample as explained in Chapter 2 (Figure 47). The amplitude cut off for all tests conducted on this sample was 60dB. The high amplitude cut off for this test can be attributed to the use of the heat capable frame MTS 816

which has less noise cancelling capability than the larger and better sound insulated frame MTS 315.

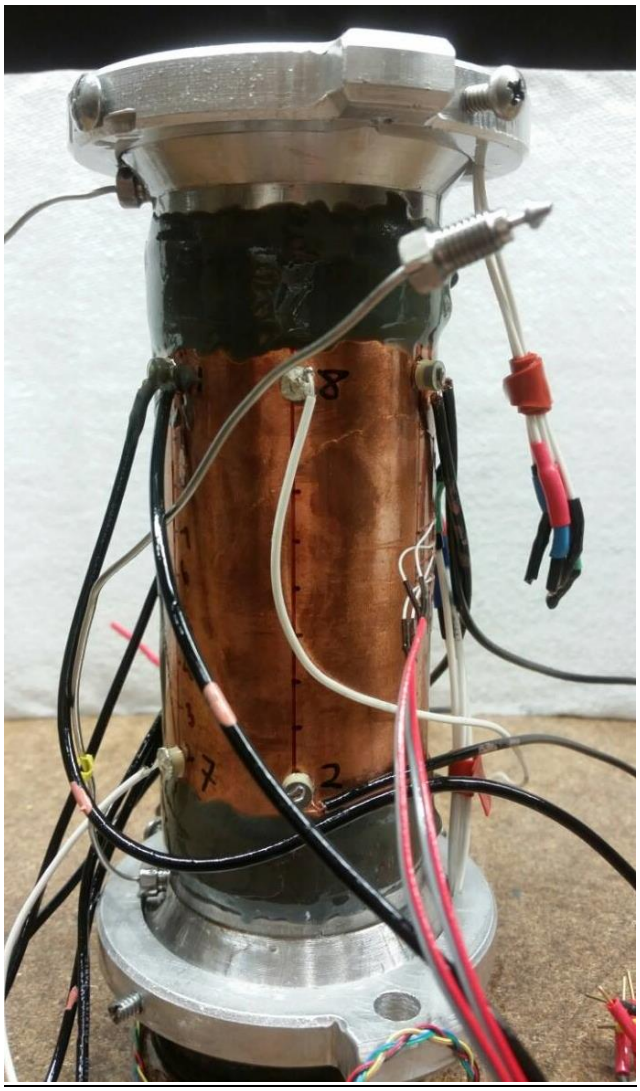

Figure 47. Sample B with Attached Acoustic Emission Crystals

The following figures (48 and 49) show the results of the Acoustic emissions for the triaxial test with confining pressure 1500 psi, the final triaxial test which resulted in sample failure. As can be seen, most of the AE events are generated during failure due to the formation of fracture as expected.

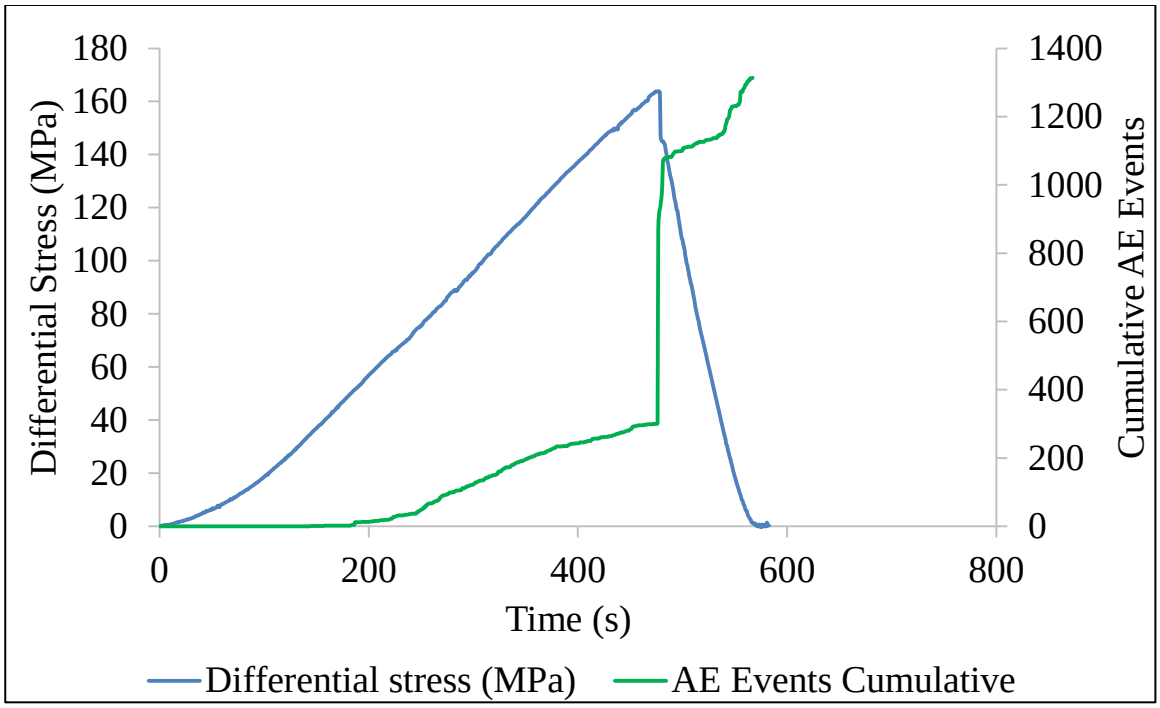

Figure 48. Differential Stress and Cumulative AE Hits vs Time for Sample B

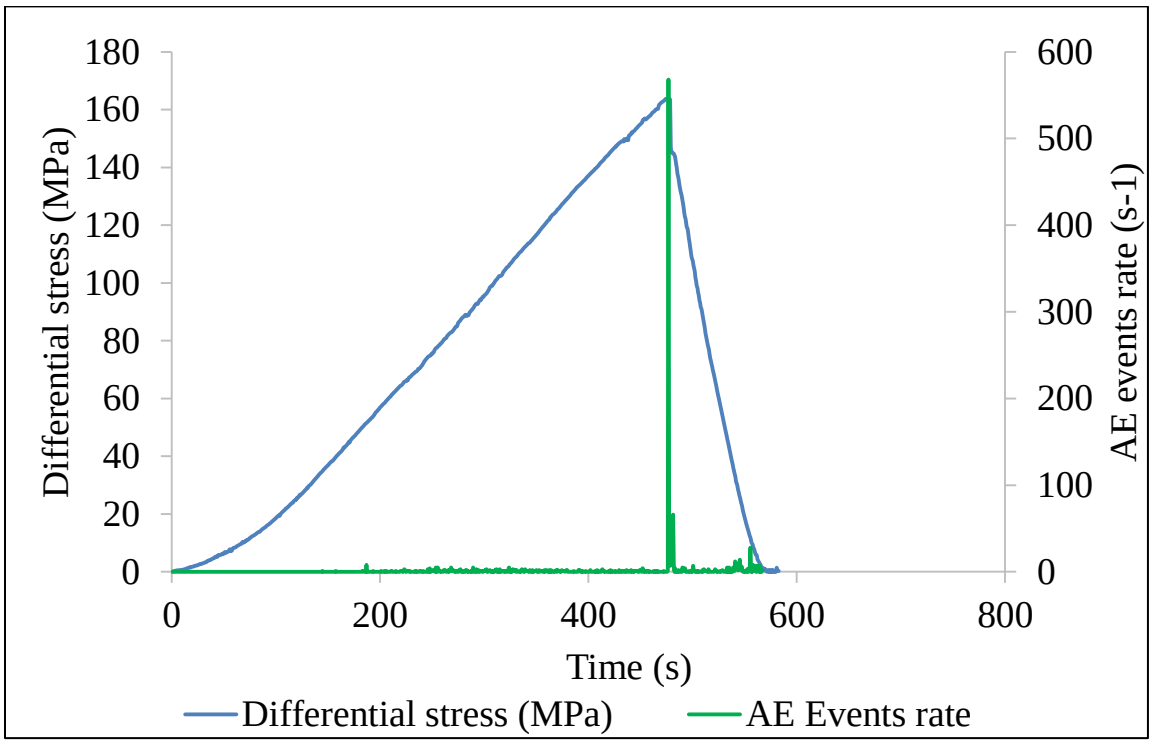

Figure 49. Differential Stress and AE Hits Rate vs Time for Sample B

The location of these events was done in 2-D as well as 3-D using MISTRAS software. This is shown in Figure 45 and 46 below. The location of events can be seen to match reasonably with the actual fracture, although location algorithm also picks up some micro-cracking events within the sample at locations further away from the fracture.

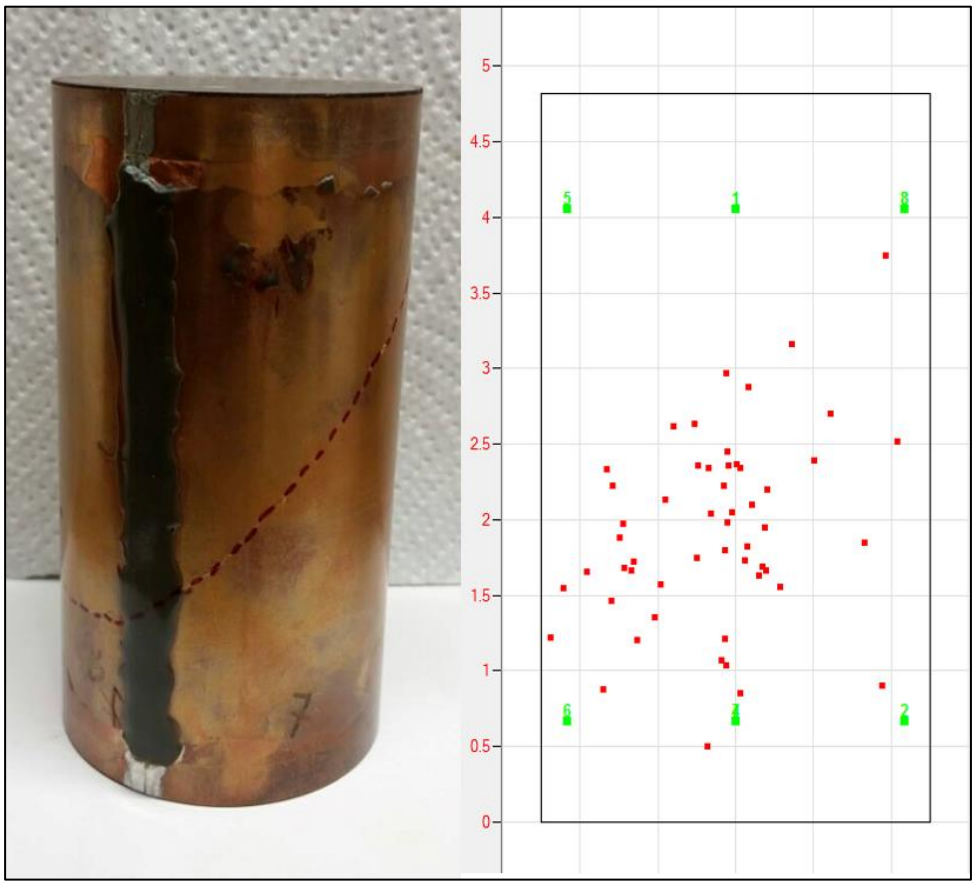

Figure 50. The Location of the Events Presented in 2-D Using MISTRAS Software beside the Fractured Sample B

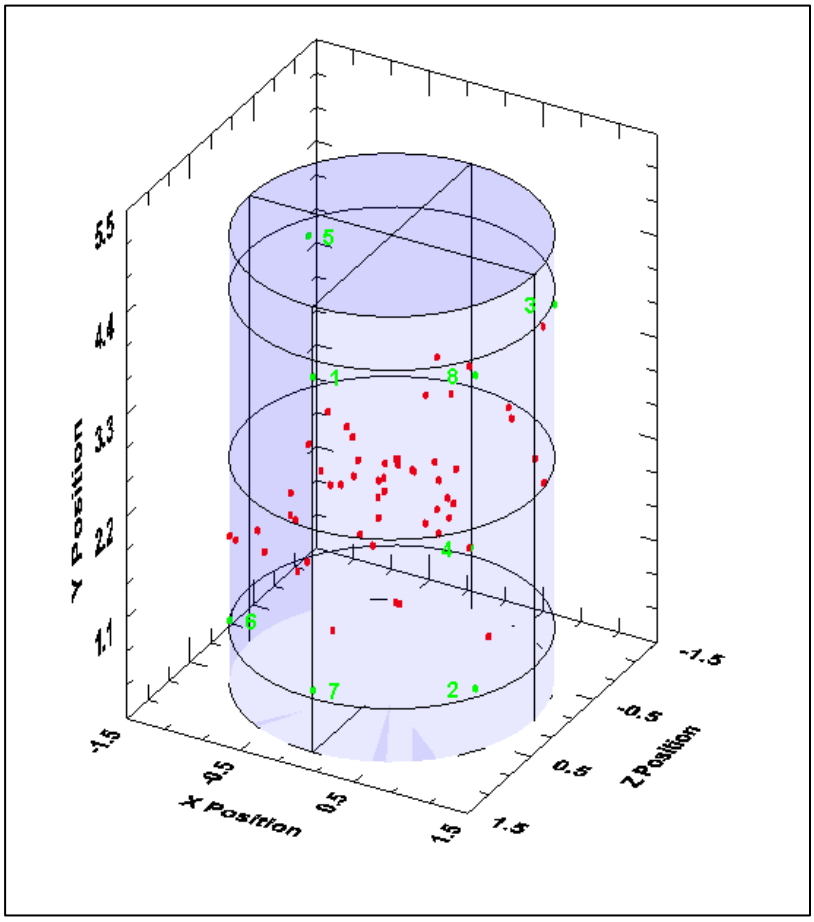

Figure 51. The Location of the Events Presented in 3-D Using MISTRAS Software for Sample B

We can see from the plots that the AE is mainly generated in the location of the fracture. The generated 3-D location is not completely accurate since it fails to pick up more events closer to the ends.

Chapter 6: Sample C - Tests, Procedures and Results

Sample Description

Sample is dark gray in color however the side of the sample is light brown full core (5892.8 – 5893.6 foot depth) and the only wok done on the core was to polish the ends to ensure parallelism of 0.1mm between the two ends. As can be seen from Figure 52 below, the outer surface wasn't highly polished at most places. The sample was cleaned with a dry cloth to remove any dust or drilling mud left on the sample. The dimensions were then measured. It has a diameter of 3.97 in (100.8 mm) and 5.6 in (142.2 mm) in length (L/D ratio of 1.41) and a bulk density of 2.67 g/cc.

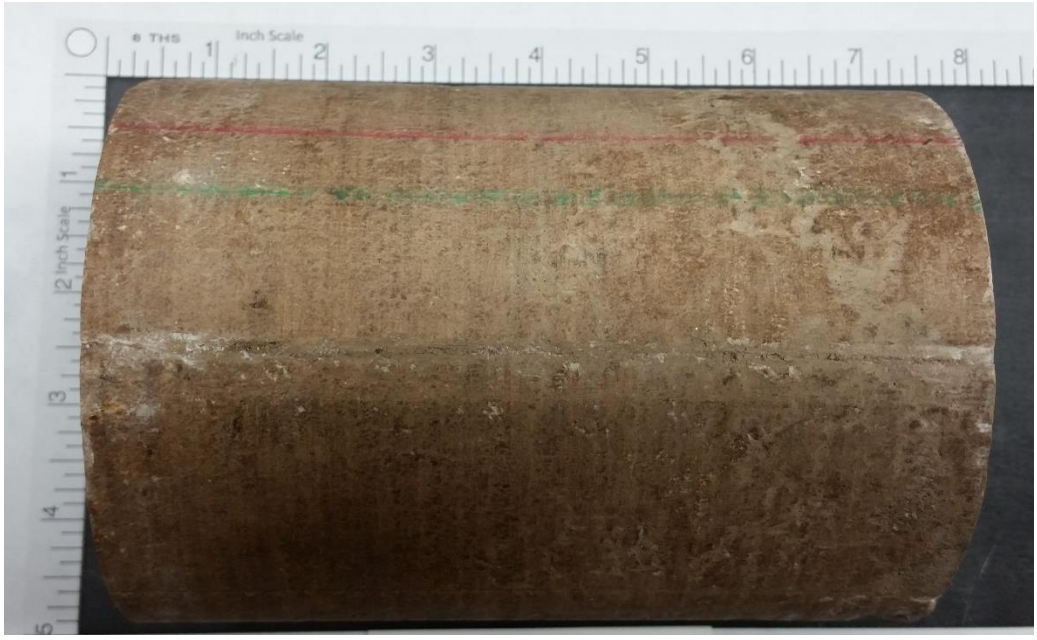

Figure 52. Sample C before Test from Second View

Having the CT scan of the core courtesy of Devon Energy shown on Figure 53, it is visible that there were not any fracture in the core initially. Note that sample core is only top 5.6 in of the full core shown on the left side of the CT scan images.

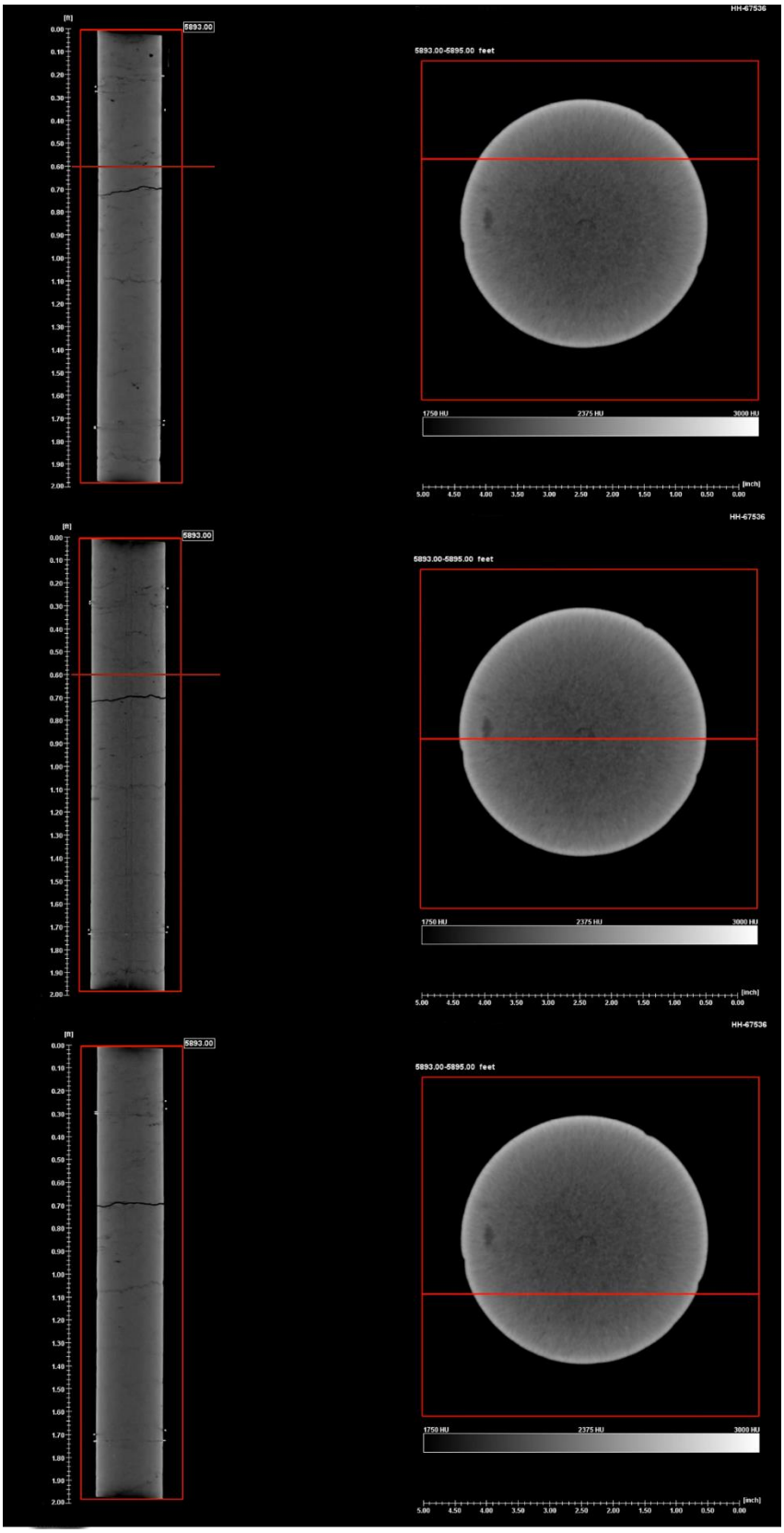

Figure 53. Side View CT Scan of Sample C at Three Different Vertical Layers

Dynamic Velocity measurements

Dynamic velocity tests were carried out with axially placed compressional and shear crystals of frequency 500 Hz. Measurements were carried out at different confining pressures. Appendix A explains how to measure the dynamic velocity. Figure 54 and Figure 55 show a screenshot of the oscilloscope measuring the P-wave and S-wave travel time for sample C at 3000 psi confining pressure. Results are summarized in Table 10 knowing that the density of the sample is 2.67 gr/cc.

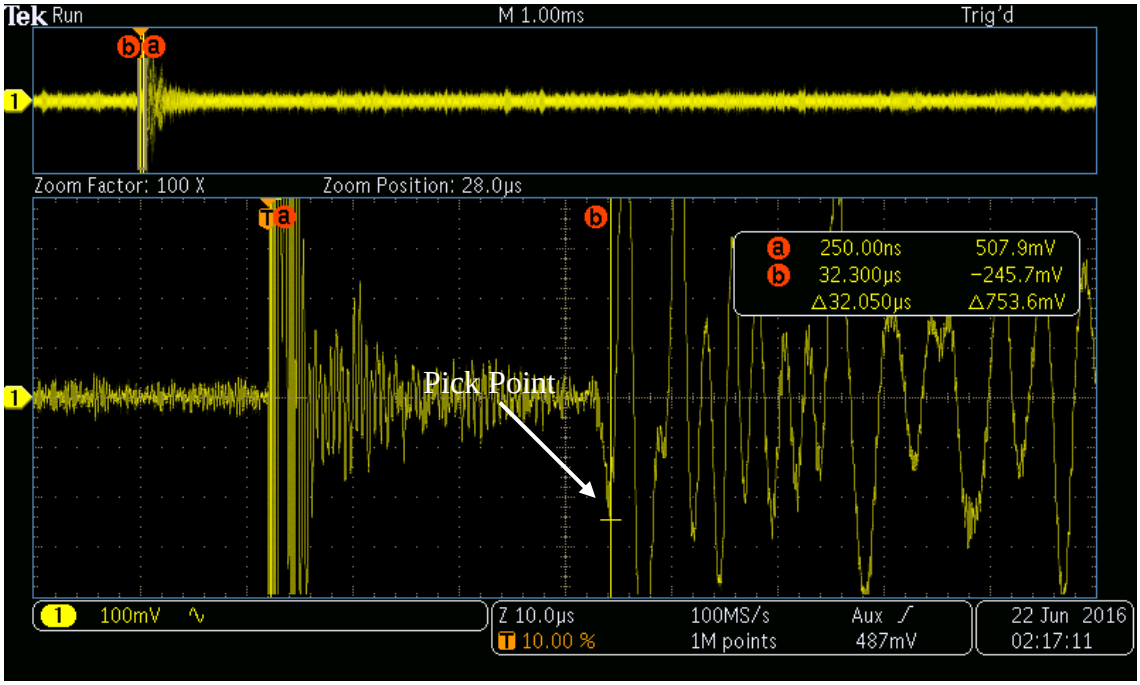

Figure 54. Screenshot of the oscilloscope measuring the P-wave travel time for sample B at 3000 psi confining pressure

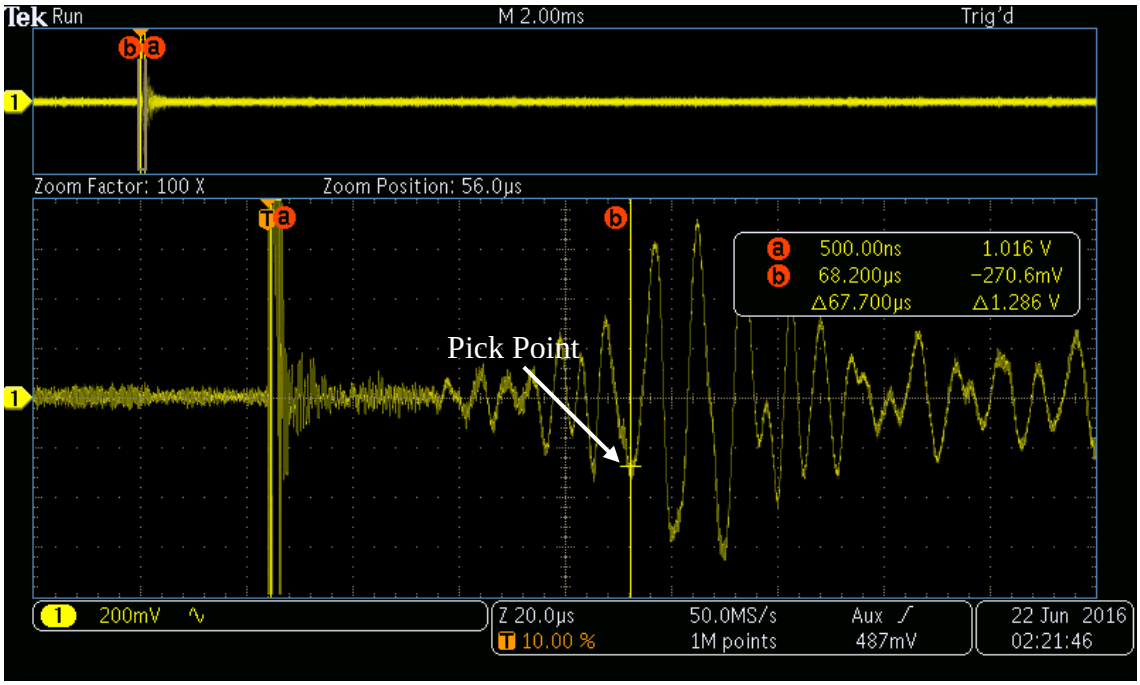

Figure 55. Screenshot of the oscilloscope measuring the S-wave travel time for sample B at 3000 psi confining pressure

Table 10. Sample C Velocity Measurements

Confining Pressure (psi)	P-wave velocity (m/s)	S-wave velocity (m/s)	Dynamic Elastic Modulus (GPa)	Dynamic Poisson's ratio
Uniaxial	3988.13	2150.80	31.93	0.29
1000	4056.38	2319.36	36.05	0.26
1500	5032.26	3001.66	58.78	0.22
2500	5274.87	3199.42	65.97	0.21

Triaxial testing and Injection

Sample C has the same objectives as previous samples which is to have a successful triaxial-injection test in mentioned conditions. Test parameters for sample C are presented in the Table 11.

Table 11. Triaxial Test Input Parameters

Specimen Type	Limestone
Specimen Diameter	100.81 mm
Specimen Length	142.2 mm
Effective Confining Pressure	2000 psi (Multistage test)
Loading method used	Strain control
Strain Loading Rate	1x10-5 strain/sec
Pore pressure differential across sample (Nitrogen)	300 psi
Strain measurements undertaken	Three strain gauges at center of sample – Two axial and one radial

Testing Results

A description of each of the tests conducted on the sample is shown below:

Room temperature test for measurement of elastic parameters

Confining pressure was increased to 2000 psi at room temperature. Sample was then loaded to a differential stress of 45 MPa at a strain rate of $1x10^{-5}$ strains/sec. and then unloaded back. Using the recorded data of the test, the differential stress is plotted versus axial strain and after adding a trend line, the slope of the trend line is calculated as the average Young's modulus of the sample which is shown in Figure 56. Also the radial strain is plotted versus axial strain and the after adding a trend line, the slope of the trend line is calculated as the Poisson's ratio of the sample which is shown in Figure 57.

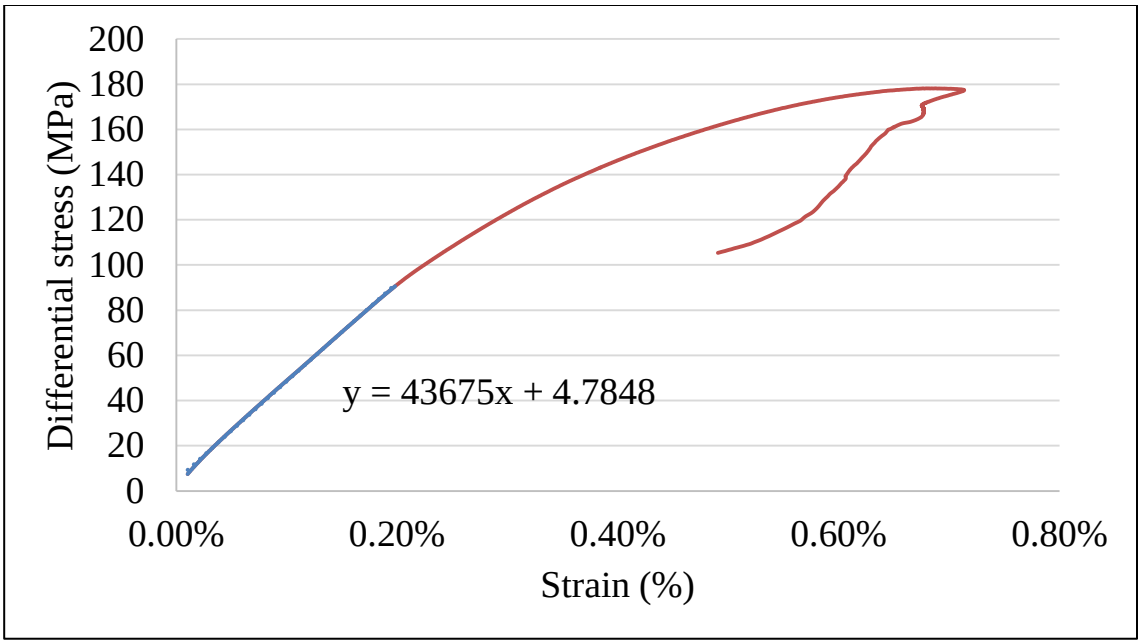

Figure 56. Stress vs Strain Plot for Sample C Conducted at 2000 psi Confining Pressure and Room Temperature for Young's Modulus Calculation.

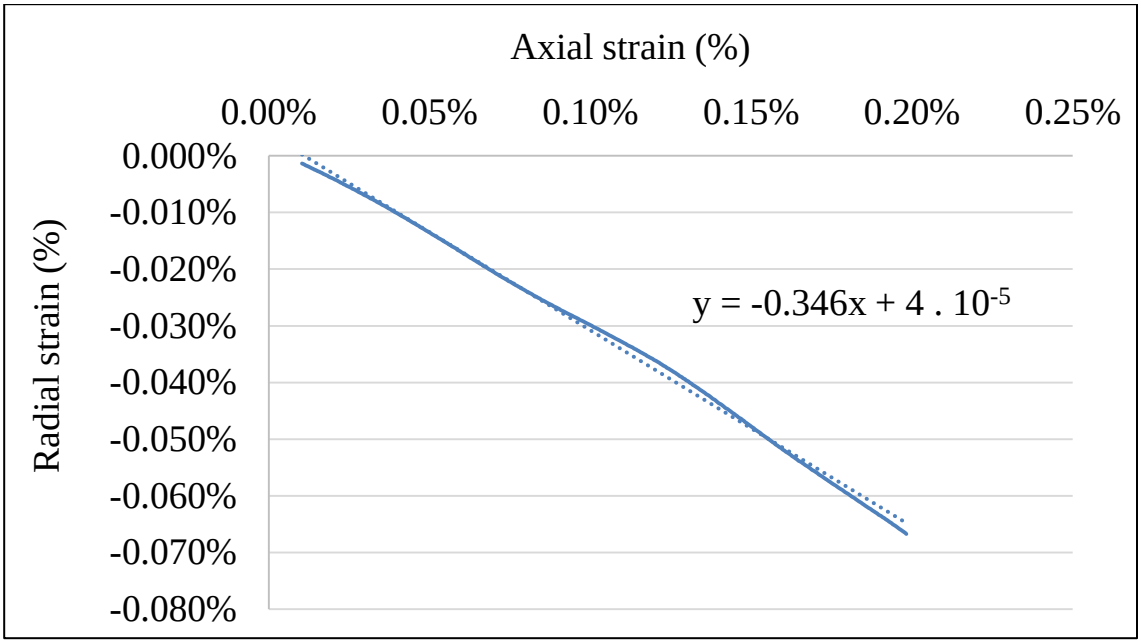

Figure 57. Radial Strain vs Axial Strain Plot for Sample C Conducted at 2000 psi Confining Pressure and Room Temperature for Poisson's Ratio Calculation.

Verifying if sample will fail due to injection

The triaxial-injection test performed on sample C in the same manner as in previous samples with the same procedure. The sample was axially loaded to a vertical stress of 6000 psi while maintaining a confining pressure of 4000 psi (Not effective) and nitrogen gas was injected at a pressure of 2000 psi resulting into an effective confining pressure of 2000 psi. Since the sample didn't fracture by injection the pore pressure was increased to 3300 psi resulting in an effective confining pressure of 700 psi. Sample C did not fractured during the triaxial-injection test. Therefore the sample was loaded axially to near dilation point (turning point of the volumetric strain curve) to be fractured by injection. However it did not get fractured by injection near the dilation point.

Triaxial-Injection test at room temperature conditions

For the last part of the test the intention was to fail the rock under triaxial-injection and not to establish a Mohr Coulomb envelope. However the sample did not get fractured by injection near the dilation point and by increasing the axil load it got fractured by compression. Figure below shows the stress strain plot for the test (Figure 58).

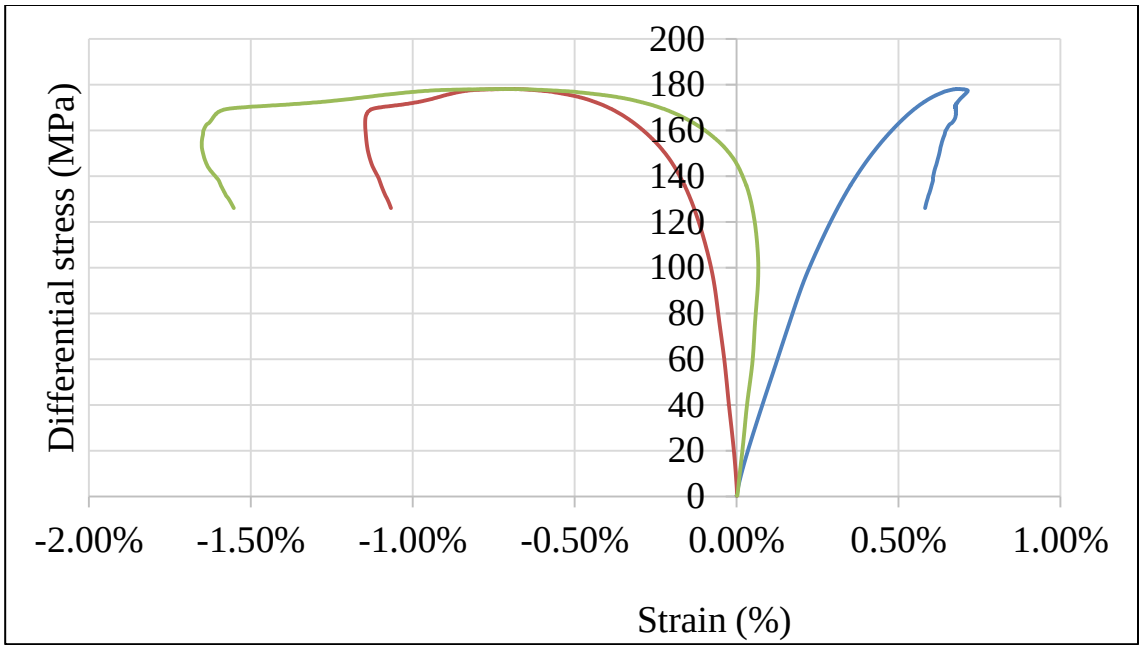

Figure 58. Differential Stress vs Strain Plot for Sample. All strains measured using strain gauges

Table 12. Results from Stress vs Strain Plots

Average Young's Modulus*	43.6 GPa
Average Poisson's ratio*	0.34
Peak Strength*	178.1 MPa
Axial strain at failure*	0.68%
Initial Permeability*	1.12 µD (micro Darcy)

* At effective confining pressure of 2000 psi

The fracture on sample C reached both ends of the sample as shown on Figure 59 in two views.

Figure 59. Sample C after Failure (Two Views)

Acoustic Emissions analysis

Eight crystals spaced placed across the sample as explained in Chapter 2 (Figure 60).

The amplitude cut off for all tests conducted on this sample was 60dB.

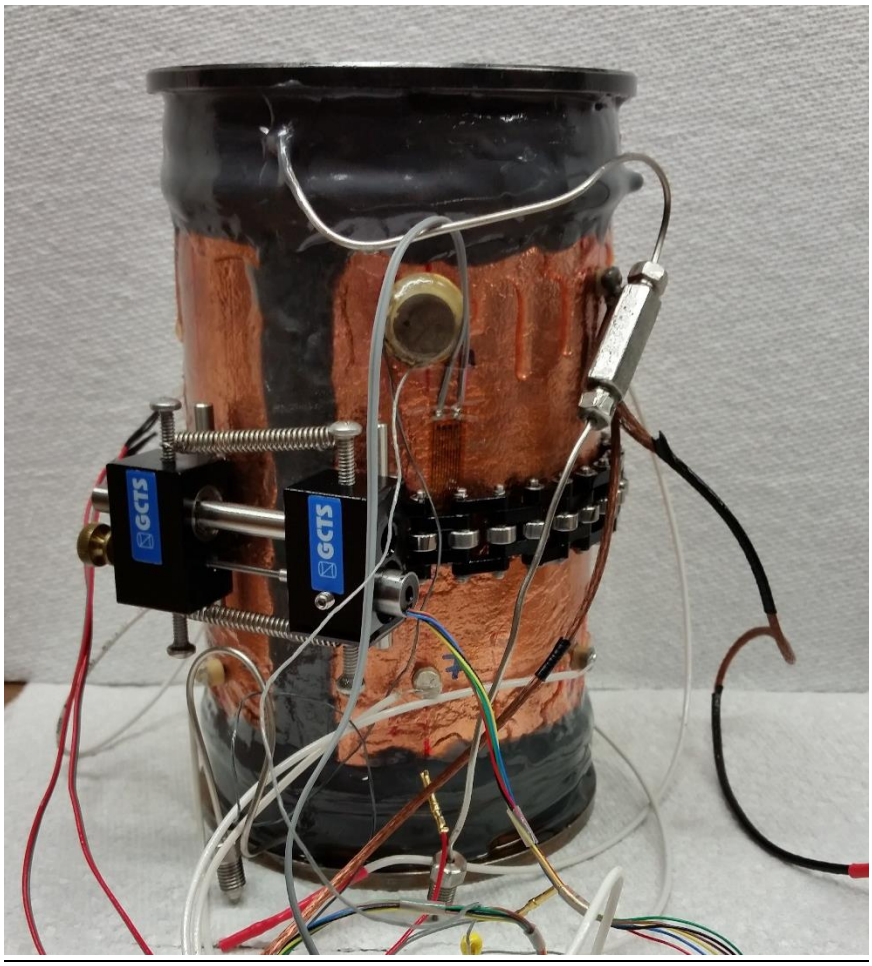

Figure 60. Sample C with Attached Acoustic Emission Crystals

The following Figures (61 and 62) show the results of the Acoustic emissions for the triaxial test with confining pressure of 2000 psi, the triaxial test which resulted in sample failure. As can be seen, most of the AE events are generated during failure due to the formation of fracture as expected.

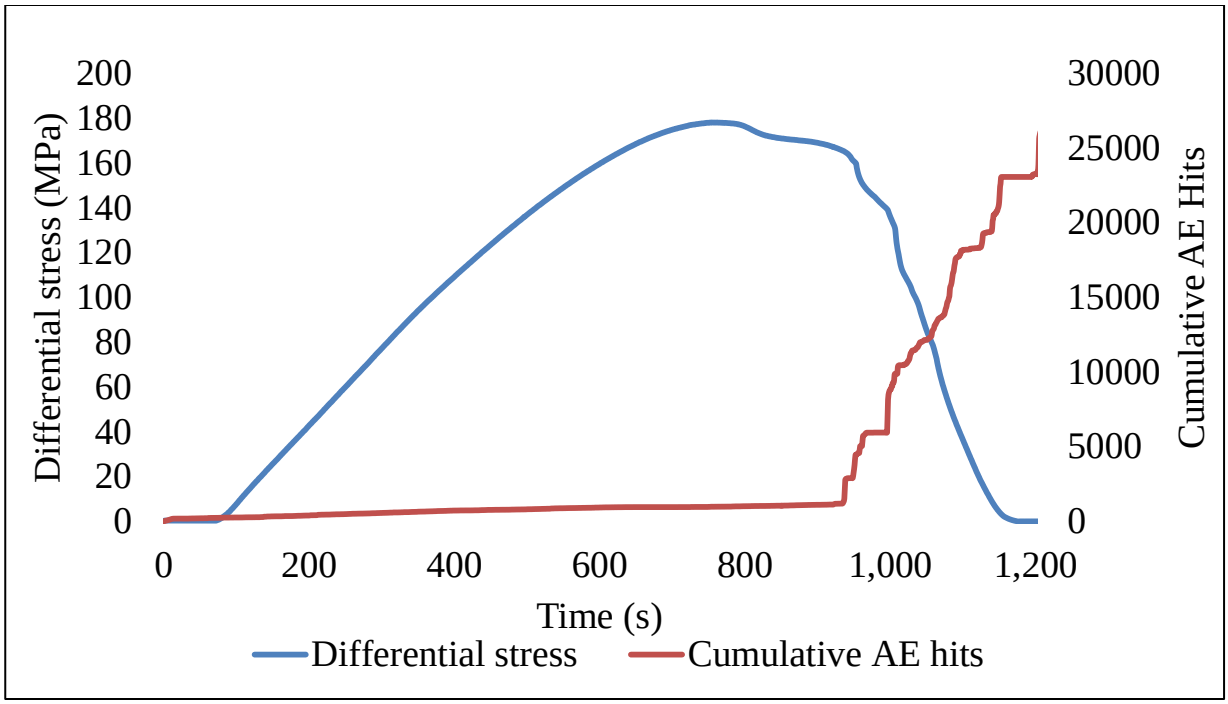

Figure 61. Differential Stress and Cumulative AE Hits vs Time for Sample C

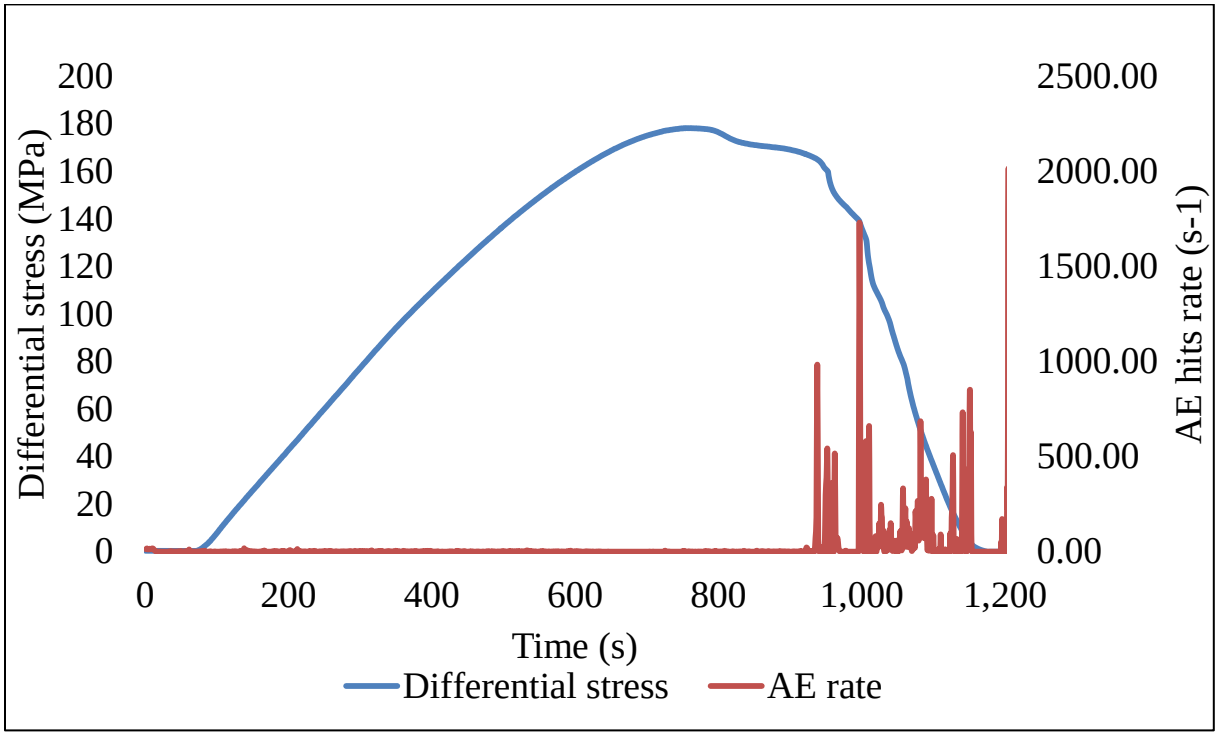

Figure 62. Differential Stress and AE Hits Rate vs Time for Sample C

The location of these events was done in 2-D as well as 3-D using MISTRAS software. This is shown in Figure 63 and 64 below. The location of events can be seen to match reasonably with the actual fracture although location algorithm also picks some micro-cracking events within the sample at locations further away from the fracture.

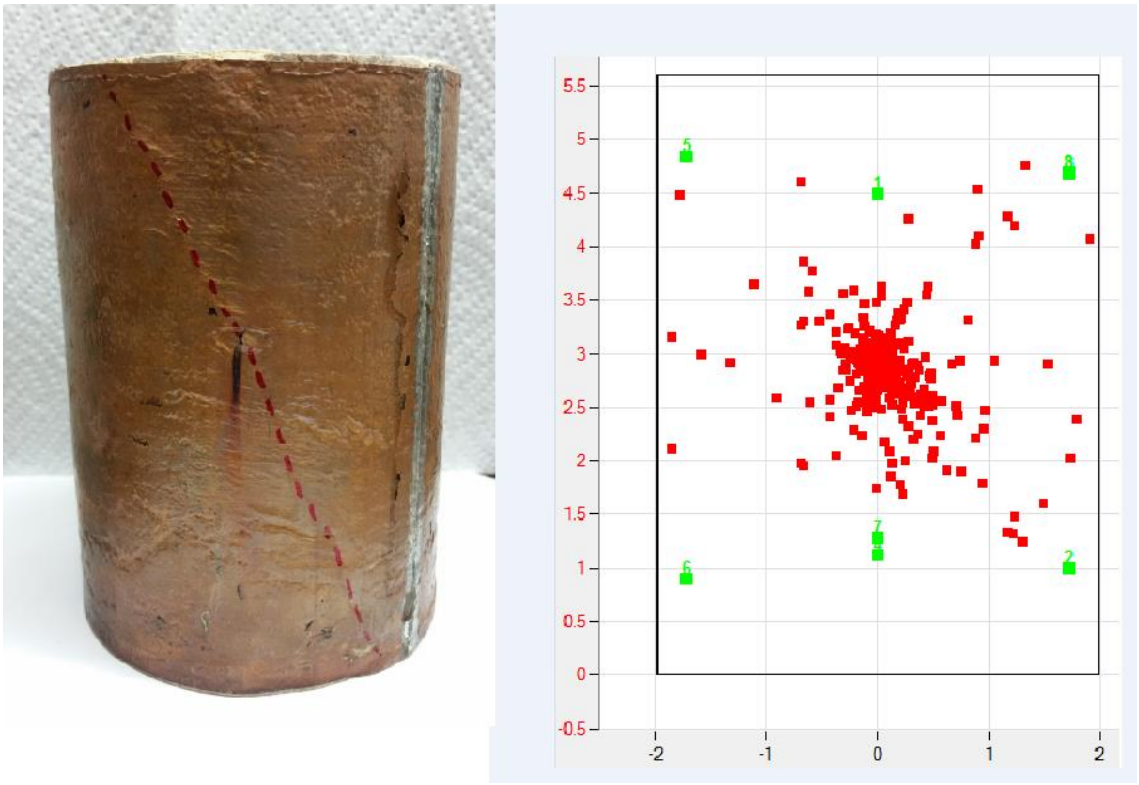

Figure 63. The Location of the Events Presented in 2-D Using MISTRAS Software beside the Fractured Sample C

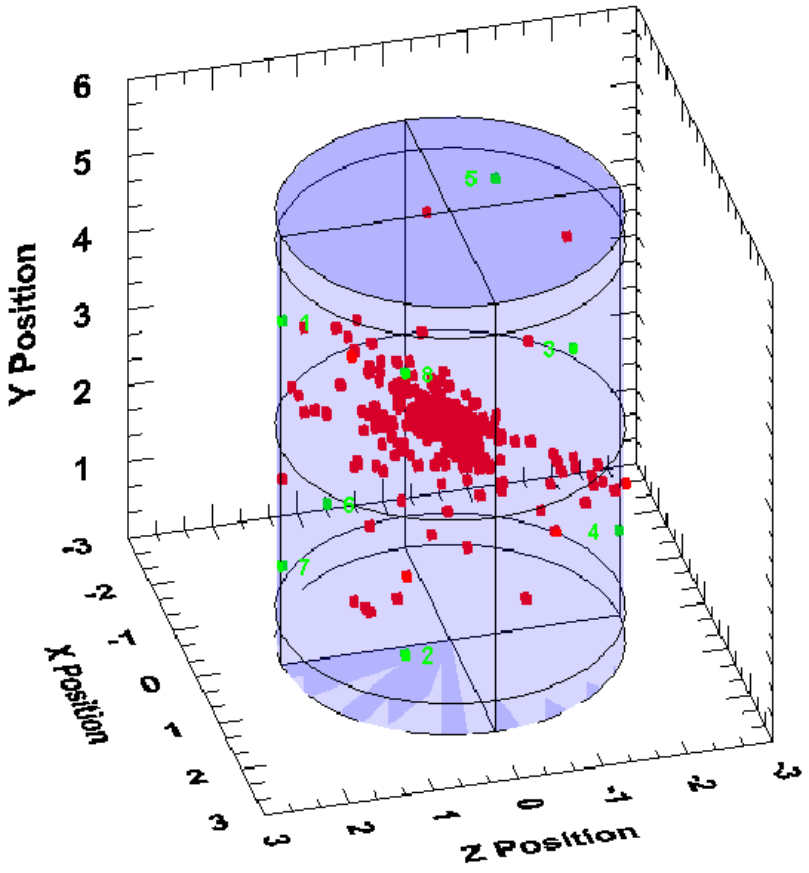

Figure 64. The Location of the Events Presented in 3-D Using MISTRAS Software for Sample C

We can see from the plots that the AE is mainly generated in the location of the fracture. The generated 3-D location is not completely accurate since it fails to pick up more events close to the ends.

Chapter 7: Conclusion

The triaxial-injection test on two GEO-N2 samples from Newberry geothermal field and Mississippi lime sample were carried out The two GEO-N2 rocks were from a depth of 10000 ft and the Mississippi lime sample was from a depth of 6000 ft. The vertical stress for testing purposes was assumed at 1 psi/ft and horizontal stress was assumed as 3500 psi ($1/3^{rd}$ of vertical stress) for two GEO-N2 samples and 2000 psi ($1/3^{rd}$ of vertical stress) for the Mississippi lime sample.

Sample A went through multi stage triaxial test after not fracturing initially by triaxial injection test. Sample B was fractured by triaxial injection however at a higher vertical load than desired. Sample C was not fractured by triaxial injection neither at the initial intended load nor at the volumetric curve turning point.

The geomechanical properties of each sample have been characterized in this work. The results provided information regarding the elastic and failure properties along with compositional analysis, and permeability. High values of Young's modulus were observed in both of the GEO N2 samples, about 41 GPa for sample A and 60 GPa for sample B. Mississippi lime sample had Young's modulus at about 43 Gpa. Permeability measurements clearly show a large increase after fracturing. AE activity was observed and recorded during the tests which matched the fractures well, exponential increase was observed near and at failure.

In terms of compressional and shear velocities, compressional velocity for sample A was on average 4800 m/s and average shear velocity was 3000 m/s, compressional velocity for sample B was on average 5400 m/s and average shear velocity was 3200

m/s, and compressional velocity for sample C was on average 4600 m/s and average shear velocity was 2600 m/s. Such high velocities exist in lower porosity rocks.

Heat didn't influence the elastic properties very much in these rocks. It is estimated that higher temperatures (>300 C) would probably create this effect.

About 0.03% strain was observed in hydrostatic heating of the sample.

Significant Acoustic emissions were observed during testing of the sample. This shows that significant MEQ's can be expected to be generated during actual fracturing. The location analysis worked well for samples B and C. This shows that location techniques need to be improved more to better understand the location of failure plane in 3-D.

References

Bakshi, R., M.E. Halvaei, A. Ghassemi. 2016. Geomechanical Characterization of Core from the Proposed FORGE Laboratory on the Eastern Snake River Plain, Idaho.

Bakshi, R., Eskandari Halvaei, M., and Ghassemi, A. Injection Experiments on Basaltic Tuffs under Triaxial and Heated Conditions with Acoustic Emissions Monitoring, ARMA 16-747, 2016.

Bargar, Keith E. and Terry E.C. Keith. 1999. Hydrothermal mineralogy of core from geothermal drill holes at Newberry Volcano, Oregon.

Crawford, A., and Wylie, D. (1987), A modified multiple failure state triaxial testing method, 28th US Rock Mechanics Symposium,133-140.

Goodman, R.E. 1989. Introduction to Rock Mechanics. 2nd ed.

Handin, J., and R. V. Hager, Experimental deformation of sedimentary rocks under confining pressure: Tests at high temperature, A.A.P.G. Bull., 42, 2892-2934, 1958.

INL/EXT-06-11746 report by MIT. 2006. The future of geothermal energy, Impact of Enhanced Geothermal Systems (EGS) on the United States in the 21st century.

Kim, M. M., and H. Y. Ko.(1979), Multistage triaxial testing of Rocks, Geotechnical Testing 2: 98-105.

Kovari, K., A. Tisa, H. Einstein, and J.A. Franklin. 1983. Suggested methods for determining the strength materials in triaxial compression, Int. J. of Rock Mech. & Min. Sci. & Geomechs Abs. 20: 283-290.

Kwasniewski, M. Mechanical behavior of rocks under true triaxial compression conditions; volumetric strain and dilatancy. Archives of

Li, Yawei, J. Wang, W. Jung, A. Ghassemi. 2012. Mechanical properties of intact rock and fractures in welded Tuff from Newberry volcano.

Petruˇza´lek M., Vilhelm J., Rudajev V., Lokajı´cˇek T., Svitek T., 2012. Determination of the anisotropy of elastic waves monitored by a sparse sensor network, International Journal of Rock Mechanics & Mining Sciences 60 (2013) 208–216

Sruoga, N. P., G. H. Rubinstein. 2004. Porosity and permeability in volcanic rocks: a case study on the Serie Tobfera, South Patagonia, Argentina, Journal of Volcanology and Geothermal Research, Volume 132, Issue 1, 15 April 2004, Pages 31-43.

Tran, D.T., Pagoulatos, A., C.H. Sondergeld. 2010. Quantify Uncertainty of Rock Failure Parameters From Laboratory Triaxial Testings Using Conventional And

Multistage Approaches, 44th U.S. Rock Mechanics Symp., June 27 - 30, 2010, Salt Lake City, Utah.

Walkey, William C., and Chandler A. Swanberg. Newberry Volcano, Oregon: new data supports conceptual hydrologic model. Geothermal Resources Council. Transactions 14 (1990): 743-748.

Appendix A - Dynamic Velocity Measurement

Dynamic velocity tests were carried within the triaxial cell just before and after the test. Velocities should be ideally measured at the in-situ conditions although measuring them at low confining pressures (500 psi at least) and then comparing those to higher pressures gives a qualitative idea of the compressibility of the material as well as its porosity. Very large differences (>10%) are seen in unconsolidated rocks while lower differences are found in consolidated rocks (<5%). The in-situ conditions for this rock was determined to be 3500 psi confining. Values below 500 psi couldn't be measured due to insufficient strength of the signal to pass through the material at lower confining pressures. In the case of all the three samples, no significant differences were observed (< 5%) for the velocities measured at 500 psi and 3500 psi. This shows the well consolidated nature of these rocks. Tests were carried out with axially placed compressional and shear crystals, both of frequency 500 Hz, placed within the top and bottom platens.

Before conducting dynamic tests, dimensions of each sample were measured and weighed; the density of each sample was then recorded. Looking at the signal reading on oscilloscope, a good signal is one where the transition from the initial noise to a high amplitude can be clearly seen without ambiguity. By measuring the travel time through the sample and subtracting the travel time from platen to platen (without a sample in between), the wave velocities of compression and shear waves through the rock were measured. The Young's modulus and Poisson's ratio based on these measurements were then recorded and reported.

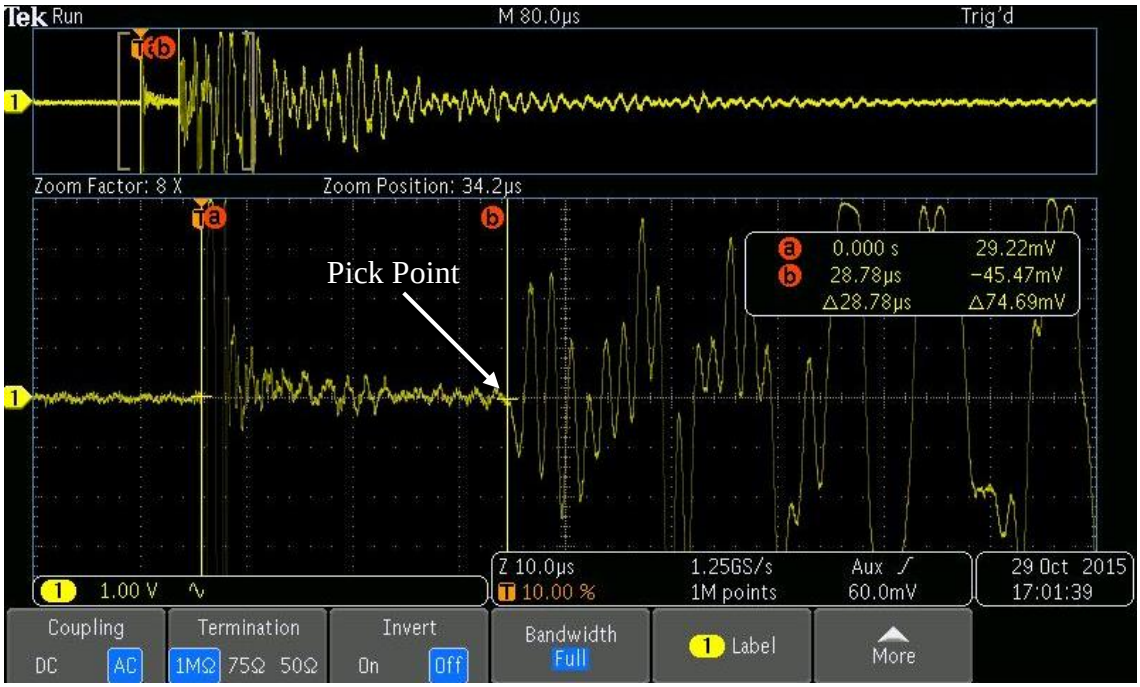

Figure 65. Oscilloscope Screen Reading the Travel Time

Appendix B - Acoustic Emission Threshold Amplitude Determination and Pencil Break Test

An amplitude filter was used for these experiments. This was selected based on the 'pencil break test'. This involves removing unwanted noise which may be present in the area due to various factors (machinery use, vibrations etc). Although efforts are made to conduct the test such that the least noise is present, some of it is inevitable and must be removed lest it gets wrongly interpreted as an AE event due to changes in rock structure. In this case, a certain amplitude was chosen and the AE monitoring switched on. If any events were observed, then higher amplitude was selected. This was done until an amplitude was reached when no events were observed for a minute. To further confirm if the crystals were functioning, a pencil lead was taken close to both ends of the platens (each housing one crystal) and broken. If a single AE event was observed, then the chosen amplitude is saved and used for the test. The pencil break test is done several times before closing the chamber as once the test starts, it is not advisable to alter it. With regards to reduction of noise so as to reduce amplitude cut off, the AE machine was grounded to the main 315 frame. See Figure 66 below, thin steel wires were taken and connected with the preamplifiers. These were then further connected to the 315 frame. It was observed that the amplitude cut-off was reduced significantly after the grounding.

Thin steel wire connected to all pre-amplifiers

Figure 66. Grounding preamplifiers on AE system